

Semi-Riemannian Graph Convolutional Networks

Bo Xiong^{1*}, Shichao Zhu^{2,5*}, Nico Potyka¹, Shirui Pan³, Chuan Zhou^{4,5}, Steffen Staab^{1,6}

¹Analytic Computing, IPVS, University of Stuttgart, Stuttgart, Germany

²Institute of Information Engineering, Chinese Academy of Sciences, Beijing, China

³Department of Data Science and AI, Faculty of IT, Monash University, Melbourne, Australia

⁴Academy of Mathematics and Systems Science, Chinese Academy of Sciences, Beijing, China

⁵School of Cyber Security, University of Chinese Academy of Sciences, Beijing, China

⁶WAIS Group, University of Southampton, Southampton, United Kingdom

{bo.xiong, nico.potyka, steffen.staab}@ipvs.uni-stuttgart.de
zhushichao@iie.ac.cn, shirui.pan@monash.edu, zhouchuan@amss.ac.cn

Abstract

Graph Convolutional Networks (GCNs) are typically studied through the lens of Euclidean geometry. Non-Euclidean Riemannian manifolds provide specific inductive biases for embedding hierarchical or spherical data, but cannot align well with data of mixed topologies. We consider a larger class of semi-Riemannian manifolds with indefinite metric that generalize hyperboloid and sphere as well as their submanifolds. We develop new geodesic tools that allow for extending neural network operations into geodesically disconnected semi-Riemannian manifolds. As a consequence, we derive a principled Semi-Riemannian GCN that first models data in semi-Riemannian manifolds of constant nonzero curvature in the context of graph neural networks. Our method provides a geometric inductive bias that is sufficiently flexible to model mixed heterogeneous topologies like hierarchical graphs with cycles. Empirical results demonstrate that our method outperforms Riemannian counterparts when embedding graphs of complex topologies.

1 Introduction

Learning from graph-structured data is a pivotal task in machine learning, for which Graph Convolutional Networks (GCNs) [1, 2, 3, 4] have emerged as powerful graph representation learning techniques. For this purpose, graphs are usually embedded in Riemannian manifolds equipped with a positive definite metric. Euclidean geometry is a special case of Riemannian manifolds of constant zero curvature that can be understood intuitively and has well-defined operations. However, the representation power of Euclidean space is limited [5], especially when embedding complex graphs exhibiting hierarchical structures [6]. Non-Euclidean Riemannian manifolds of constant curvatures provide an alternative to accommodate specific graph topologies such as hierarchical or cyclical structures. An intuitive example is a hyperbolic manifold of constant negative curvature that is well suited to represent hierarchical structures such as tree-like graphs [7, 8]. Similarly, spherical manifold of constant positive curvature can be used to model spherical data in various fields [9, 10, 11]. Some recent works [12, 13, 14, 15] have extended GCNs to such non-Euclidean manifolds and have shown substantial improvements when embedding into specific geometries.

The topologies in real-world graphs [6], however, usually exhibit highly heterogeneous topological structures, which are best represented by different geometrical curvatures. A globally homogeneous geometry lacks the flexibility for modeling complex graphs, resulting in distortional representations. Instead of using a single manifold, product manifolds [16, 17], combining multiple Riemannian manifolds have shown advantages when embedding graphs of mixed topologies. But the simple

*Equal contributions.

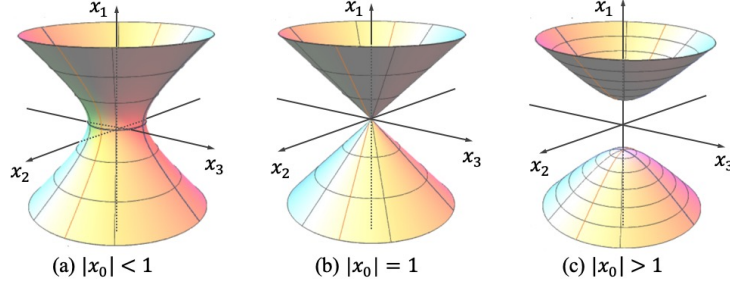


Figure 1: The different submanifolds of a four-dimensional pseudo-hyperboloid of curvature -1 with two time dimensions. By fixing one time dimension x_0 , the induced submanifolds include (a) an one-sheet hyperboloid, (b) the double cone, and (c) a two-sheet hyperboloid.

combination of spaces still does not accommodate topologically heterogeneous graphs very well. Furthermore, Riemannian manifolds are equipped with a positive definite metric disallowing for the faithful representation of the negative eigen-spectrum of input similarities [18].

Going beyond Riemannian manifolds, semi-Riemannian manifolds equipped with indefinite metric constitute a larger class of geometries. Semi-Riemannian manifolds of constant nonzero curvature do not only generalize the hyperbolic and spherical manifolds, but also contain their submanifolds (Cf. Fig. 1), thus providing inductive biases specific to these geometries. Semi-Riemannian geometry with constant zero curvature (pseudo-Euclidean space) was first applied [5] to manifold learning for preserving local information of non-metric data. To model complex graphs containing both hierarchies and cycles, semi-Riemannian manifolds with constant nonzero curvature (pseudo-hyperboloid) have recently been applied into graph embeddings using shallow learning [19], but the representation power of these works is not on par with the Riemannian counterparts yet, mostly because of the absence of geodesic tools to extend neural network operations into semi-Riemannian geometry.

In this paper, we take the first step to extend GCNs into semi-Riemannian manifolds foregoing the requirement to have a positive definite metric. Exploiting semi-Riemannian geometry for GCNs is non-trivial because of the *geodesical disconnectedness* in semi-Riemannian geometry. There exist broken points that cannot be smoothly connected by a geodesic, leaving necessary geodesic tools undefined. To deal with it, we develop novel geodesic tools that empower manipulating representations in geodesically disconnected semi-Riemannian manifolds. We make it by finding diffeomorphic manifolds that provide alternative geodesic operations that smoothly avoid the broken cases. Subsequently, we generalize GCNs to learn representations of complex graphs in semi-Riemannian geometry by defining corresponding operations such as *linear transformation* and *tangential aggregation*. We have shown that our representations are well adapted to the more general case of mixed topological structures, such as hierarchical graphs with cycles.

To summarize, the main contributions of this paper are as follows.

- To the best of our knowledge, we are the first to define neural network operations in semi-Riemannian manifolds with novel geodesic tools, to stimulate the applications of semi-Riemannian geometry in geometric deep learning.
- We present a principled framework, Semi-Riemannian GCN, which generalizes GCNs into semi-Riemannian manifolds with indefinite metrics, providing more flexible inductive biases to accommodate complex graphs with mixed topologies.
- Extensive evaluations on three standard tasks demonstrate that our model outperforms baselines which operate in Riemannian manifolds. Code and data have been submitted anonymously at <https://github.com/QGCN/QGCN>.

2 Preliminaries

Semi-Riemannian manifolds. A semi-Riemannian (or pseudo-Riemannian) manifold [20] (\mathcal{M}, g) is a smooth manifold \mathcal{M} equipped with a non-degenerate and indefinite metric tensor g . The metric tensor g induces a scalar product on *tangent space* $\mathcal{T}_{\mathbf{x}}\mathcal{M}$ for each point $\mathbf{x} \in \mathcal{M}$ such that $g_{\mathbf{x}} : \mathcal{T}_{\mathbf{x}}\mathcal{M} \times \mathcal{T}_{\mathbf{x}}\mathcal{M} \rightarrow \mathbb{R}$, where the *tangent space* $\mathcal{T}_{\mathbf{x}}\mathcal{M}$ is a vector space and can be seen as a first

order local approximation of \mathcal{M} around point \mathbf{x} . The elements of $\mathcal{T}_{\mathbf{x}}\mathcal{M}$ are called the tangent vectors. A principal special case is Riemannian geometry, where the metric is positive definite [20, 21]. Please refer to Appendix C and Appendix D for more details.

Pseudo-hyperboloid. By analogy with hyperboloid and sphere in Euclidean space. Pseudo-hyperboloids are defined as the submanifolds in the ambient pseudo-Euclidean space $\mathbb{R}^{s,t+1}$ with the dimensionality of $d = s + t + 1$ that uses the scalar product as Eq. (1). The scalar product induces a norm $\|\mathbf{x}\|_t^2 = \langle \mathbf{x}, \mathbf{x} \rangle_t$ that can be used to define a pseudo-hyperboloid $\mathcal{Q}_\beta^{s,t}$ as Eq. (2).

$$\forall \mathbf{x}, \mathbf{y} \in \mathbb{R}^{s,t+1}, \langle \mathbf{x}, \mathbf{y} \rangle_t = - \sum_{i=0}^t x_i y_i + \sum_{j=t+1}^{s+t} x_j y_j. \quad (1)$$

$$\mathcal{Q}_\beta^{s,t} = \left\{ \mathbf{x} = (x_0, x_1, \dots, x_{s+t})^\top \in \mathbb{R}^{s,t+1} : \|\mathbf{x}\|_t^2 = \beta \right\}, \quad (2)$$

where β is the nonzero real number parameter of curvature. $\mathcal{Q}_\beta^{s,t}$ is called a *pseudo-sphere* when $\beta > 0$ and a *pseudo-hyperboloid* when $\beta < 0$. Since $\mathcal{Q}_\beta^{s,t}$ is interchangeable with $\mathcal{Q}_{-\beta}^{t+1,s-1}$, we will only consider the pseudo-hyperboloid case. Following the terminology of special relativity, a point in $\mathcal{Q}_\beta^{s,t}$ can be interpreted as an event [5], where the first $t + 1$ dimensions are time dimensions and the last s dimensions are space dimensions. Hyperbolic and spherical manifolds can be defined as the special cases of pseudo-hyperboloids by setting all time dimensions except one to be zero and setting all space dimensions to be zero, respectively, i.e. $\mathbb{H}_\beta = \mathcal{Q}_\beta^{s,1}$, $\mathbb{S}_\beta = \mathcal{Q}_\beta^{0,t}$.

Geodesic, exponential map and logarithmic map. A geodesic is a locally length-minimizing curve connecting points \mathbf{x} and \mathbf{y} on the manifold, formally given by $\gamma_{\mathbf{x} \rightarrow \boldsymbol{\xi}}(\tau) : I \rightarrow \mathcal{M}$ from an interval $I = [0, 1]$ to the metric space \mathcal{M} with direction $\boldsymbol{\xi}$. The reached point \mathbf{y} can be then defined as $\mathbf{y} = \gamma_{\mathbf{x} \rightarrow \boldsymbol{\xi}}(\tau)$. The geodesics of pseudo-hyperboloid are a combination of the hyperbolic, flat and spherical cases, corresponding to time-like, light-like and space-like geodesics [22]. The geodesic works as an essential tool to define mappings between manifolds and tangent spaces. By the means of geodesic, exponential map can be defined as $\text{expmap} : \gamma_{\mathbf{x} \rightarrow \boldsymbol{\xi}}(1)$, which maps tangent vectors to the manifold. Note that $\mathcal{Q}_\beta^{s,t}$ is a *geodesically complete* manifold, which means that the expmap is defined on the entire tangent space, i.e. $\text{exp}_\mathbf{x}^\beta(\cdot) : \mathcal{T}_\mathbf{x}\mathcal{Q}_\beta^{s,t} \rightarrow \mathcal{Q}_\beta^{s,t}$. The logmap $\text{log}_\mathbf{x}^\beta(\cdot) : \mathcal{Q}_\beta^{s,t} \rightarrow \mathcal{T}_\mathbf{x}\mathcal{Q}_\beta^{s,t}$ can be defined as the inverse of the expmap . Details on the *geodesic*, *expmap* and *logmap* in pseudo-hyperboloid can be found in the Appendix C.

Geodesical connectedness. A semi-Riemannian manifold \mathcal{M} is *connected* iff any two points of \mathcal{M} can be joined by a piecewise (broken) geodesic with each piece being a smooth geodesic. The manifold is *geodesically connected* (or *g-connected*) iff any two points can be smoothly connected by a geodesic, where the two points are called *g-connected*, otherwise called *g-disconnected*.

Different from Riemannian manifolds in which the geodesical completeness implies the *g-connectedness* (Hopf–Rinow theorem [23]), pseudo-hyperboloid is a geodesically complete but not *g-connected* manifold where there exist points that cannot be smoothly connected by a geodesic. Please refer standard books [24, 25] for details. In pseudo-hyperboloid, two points $\mathbf{x}, \mathbf{y} \in \mathcal{Q}_\beta^{s,t}$ are *g-connected* iff $\langle \mathbf{x}, \mathbf{y} \rangle_t < |\beta|$. The set of *g-connected* points of $\mathbf{x} \in \mathcal{Q}_\beta^{s,t}$ is denoted as its *normal neighborhood* $\mathcal{U}_\mathbf{x} = \left\{ \mathbf{y} \in \mathcal{Q}_\beta^{s,t} : \langle \mathbf{x}, \mathbf{y} \rangle_t < |\beta| \right\}$. For *g-disconnected* points $\mathbf{x}, \mathbf{y} \in \mathcal{Q}_\beta^{s,t}$, there does not exist a tangent vector $\boldsymbol{\xi}$ such that $\mathbf{y} = \text{exp}_\mathbf{x}^\beta(\boldsymbol{\xi})$, which implies that its inverse $\text{log}_\mathbf{x}^\beta(\cdot)$ is only defined in the *normal neighborhood* of \mathbf{x} . In a nutshell, the geodesic tools for the *g-disconnected* cases are not well-defined, making it impossible to define corresponding vector operations.

3 Geodesic Tools on Pseudo-Hyperboloid

3.1 Diffeomorphism of Pseudo-Hyperboloid

One standard way to tackle the *intractability* in differential geometry is to perform operations on their diffeomorphic manifolds that are easier to manipulate.

Definition 3.1 (Diffeomorphism [20]). *Given two manifolds \mathcal{M} and \mathcal{M}' , a smooth map $\psi : \mathcal{M} \rightarrow \mathcal{M}'$ is called a diffeomorphism if ψ is bijective and its inverse ψ^{-1} is smooth as well. If a diffeomorphism between \mathcal{M} and \mathcal{M}' exists, we call them diffeomorphic and write $\mathcal{M} \simeq \mathcal{M}'$.*

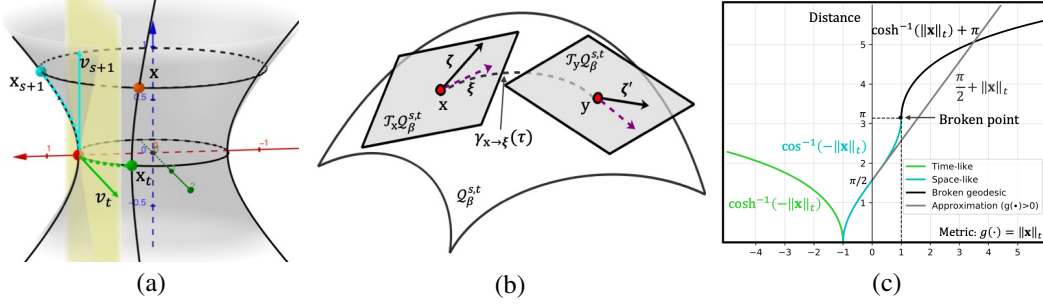


Figure 2: (a) Hyperbolic projection (cyan) and spherical projection (green) map the point x (red) to tangent vectors v_{s+1} and v_t , respectively. (b) The parallel transport $P_{x \rightarrow y}^\beta(\xi)$ moves tangent vector $\zeta \in \mathcal{T}_x Q_\beta^{s,t}$ to the tangent space $\mathcal{T}_y Q_\beta^{s,t}$ with the tangent direction ξ . (c) The piecewise geodesic distance (green, cyan and black) and the approximation part (gray).

For semi-Riemannian manifolds, following diffeomorphism [19] decomposes pseudo-hyperboloid into the product manifolds of an unit sphere and the Euclidean space.

Theorem 3.1 (Theorem 4.1 in [19]). *For any point $x \in Q_\beta^{s,t}$, there exists a diffeomorphism $\psi : Q_\beta^{s,t} \rightarrow \mathbb{S}_1^t \times \mathbb{R}^s$ that maps x into the product manifolds of an unit sphere and the Euclidean space.*

Inspired by this, we present two dual diffeomorphisms that map x into the product manifolds of sphere with curvature $-1/\beta$ (resp. hyperboloid with curvature $1/\beta$) and the Euclidean space.

Theorem 3.2. *For any point $x \in Q_\beta^{s,t}$, there exists a diffeomorphism $\psi : Q_\beta^{s,t} \rightarrow \mathbb{S}_{-\beta}^t \times \mathbb{R}^s$ that maps x into the product manifolds of a sphere and the Euclidean space (proof in Appendix E.2).*

Theorem 3.3. *For any point $x \in Q_\beta^{s,t}$, there exists a diffeomorphism $\psi : Q_\beta^{s,t} \rightarrow \mathbb{R}^{t-1} \times \mathbb{H}_\beta^{s+1}$ that maps x into the product manifolds of the Euclidean space and hyperboloid¹ (proof in Appendix E.3).*

Compared with Theorem 3.1, the two diffeomorphisms preserve the curvatures in their diffeomorphic components, which is more intuitively understandable. Theorem 3.2 and Theorem 3.3 yield spherical projection (denoted by ψ_s) and hyperbolic projection (denoted by ψ_H), respectively (Cf. Fig. 2(a)). The projections satisfy some geometric properties, e.g. the mapped points $x_t \in \mathbb{S}_{-\beta}^t$ and $x_{s+1} \in \mathbb{H}_\beta^{s+1}$ still lie on the surface of the pseudo-hyperboloid (Cf. Fig. 2(a)). Furthermore, these two dual diffeomorphisms offer an insight to interpret the geometric properties of the embeddings. For example, to interpret the hierarchical structures of the embeddings, we can conduct the projection $\psi_H : Q_\beta^{s,t} \rightarrow \mathbb{R}^{t-1} \times \mathbb{H}_\beta^{s+1}$ and visualize the hyperbolic component \mathbb{H}_β^{s+1} .

In fact, by generalizing Theorem 3.2 and Theorem 3.3, we present a more flexible diffeomorphism that decomposes pseudo-hyperboloid into the product manifolds.

Theorem 3.4 (Decomposability). *For any point $x \in Q_\beta^{s,t}$ ($s > 0, t > 1$), and two integers $a \in [0, s], b \in [1, t]$, there exists a diffeomorphism $\psi : Q_\beta^{s,t} \rightarrow \mathbb{R}^{t-b} \times Q_\beta^{a,b} \times \mathbb{R}^{s-a}$ that maps $Q_\beta^{s,t}$ to the product manifolds of the Euclidean space and its submanifold (proof in Appendix E.4).*

In this case, Theorem 3.2 and Theorem 3.3 can be seen as two special cases by setting $a = 0, b = t$ and $a = s, b = 1$, respectively. Another more special case by setting $a = 0, b = 1$ induces a 0-sphere, the detail is shown in the Appendix F.1.

The Theorem 3.4 provides *decomposability* as an alternative way to analyze and manipulate the geodesics when the geodesic tools are not well-defined in pseudo-hyperboloid. However, Theorem 3.5 shows that not all diffeomorphic manifolds in Theorem 3.4 are *g-connected*.

Theorem 3.5. *For the pseudo-hyperboloid $Q_\beta^{s,t}$ ($s > 0, t > 1$), the corresponding diffeomorphic manifold $\mathbb{R}^{t-b} \times Q_\beta^{a,b} \times \mathbb{R}^{s-a}$ is *g-connected* iff $a = 0$ and $b \in (1, t]$ (proof in Appendix E.5).*

¹Note that here we use \mathbb{H}_β to denote the double-sheet hyperboloid (see Fig. 1 (c)). In the literature, the upper-sheet hyperboloid is usually defined by $\mathbb{H}_\beta(x_0 > 0)$ or \mathbb{H}_β^+ .

The intuition is that we must project all space dimensions to \mathbb{R} , as the space dimension will induce hyperbolic submanifolds that contain two isolated sheets, which are obviously disconnected (see Fig. 1 (c)). For time dimension, the setting $b = 1$ induces 0-sphere consisting of two isolated points. Thus, the diffeomorphic manifolds are only g -connected under the settings $a = 0, b \in (1, t]$.

3.2 Geodesic Tools for G-disconnected Pseudo-hyperboloid

Exponential and logarithmic map. As the pseudo-hyperboloid $\mathcal{Q}_\beta^{s,t}$ is g -disconnected, we transfer the $\log\text{map}$ and $\exp\text{map}$ into the diffeomorphic manifolds. Considering the g -connectedness and the computation efficiency, we use the spherical diffeomorphism $\psi_\mathbb{S} : \mathcal{Q}_\beta^{s,t} \rightarrow \mathbb{S}_{-\beta}^t \times \mathbb{R}^s$ by setting $b = t$. The new $\log\text{map}$ and its inverse $\exp\text{map}$ can be defined by Eq. (3).

$$\widehat{\log}_{\mathcal{Q}_\beta^{s,t}}(\mathbf{x}) = \log_{\mathbb{S}_{-\beta}^t \times \mathbb{R}^s}(\psi_\mathbb{S}(\mathbf{x})), \quad \widehat{\exp}_{\mathcal{Q}_\beta^{s,t}}(\boldsymbol{\xi}) = \psi_\mathbb{S}^{-1}(\exp_{\mathbb{S}_{-\beta}^t \times \mathbb{R}^s}(\boldsymbol{\xi})), \quad (3)$$

where $\psi_\mathbb{S}(\cdot)$ is the spherical projection and $\psi_\mathbb{S}^{-1}(\cdot)$ is the inverse. $\log_{\mathbb{S}_{-\beta}^t \times \mathbb{R}^s}(\cdot)$ and $\exp_{\mathbb{S}_{-\beta}^t \times \mathbb{R}^s}(\cdot)$ in the product manifolds can be defined as the concatenation of corresponding operations.

$$\log_{\mathbb{S}_{-\beta}^t \times \mathbb{R}^s}(\mathbf{x}') = \log_{\mathbb{S}_{-\beta}^t}(\mathbf{x}'_t) \parallel \log_{\mathbb{R}^s}(\mathbf{x}'_s), \quad \exp_{\mathbb{S}_{-\beta}^t \times \mathbb{R}^s}(\boldsymbol{\xi}) = \exp_{\mathbb{S}_{-\beta}^t}(\boldsymbol{\xi}_t) \parallel \exp_{\mathbb{R}^s}(\boldsymbol{\xi}_s), \quad (4)$$

where \parallel denotes the concatenation, $\mathbf{x}' = \psi_\mathbb{S}(\mathbf{x})$ that consists of spherical features $\mathbf{x}'_t \in \mathbb{S}_{-\beta}^t$ and Euclidean features $\mathbf{x}'_s \in \mathbb{R}^s$. $\boldsymbol{\xi}$ is the tangent vector induced by \mathbf{x}' with $\boldsymbol{\xi}_t \in \mathcal{T}_{\mathbf{x}'_t} \mathbb{S}_{-\beta}^t$ and $\boldsymbol{\xi}_s \in \mathbb{R}^s$.

Although we transfer $\log\text{map}$ and $\exp\text{map}$ to the diffeomorphic manifold $\mathbb{S}_{-\beta}^t \times \mathbb{R}^s$, the diffeomorphic operations $\widehat{\log}_\mathbf{x}(\cdot)$ and $\widehat{\exp}_\mathbf{x}(\cdot)$ at the reference point \mathbf{x} with zero space dimension are *intrinsic*, which means they are bijective functions from points on the pseudo-hyperboloid to the tangent space induced by \mathbf{x} , asserted by Theorem 3.6.

Theorem 3.6 (Diffeomorphic operations are intrinsic). *For any reference point $\mathbf{x} = \begin{pmatrix} \mathbf{t} \\ \mathbf{s} \end{pmatrix} \in \mathcal{Q}_\beta^{s,t}$ with space dimension $\mathbf{s} = \mathbf{0}$, the induced tangent space of $\mathcal{Q}_\beta^{s,t}$ is equal to the tangent space of its diffeomorphic manifold $\mathbb{S}_{-\beta}^t \times \mathbb{R}^s$, namely, $\mathcal{T}_\mathbf{x}(\mathbb{S}_{-\beta}^t \times \mathbb{R}^s) = \mathcal{T}_\mathbf{x} \mathcal{Q}_\beta^{s,t}$. (proof in the Appendix E.6).*

Remarkably, the *intrinsicity* of the diffeomorphic operations make them preserve the geometric expressiveness of pseudo-hyperboloid. This is different from product manifolds that manipulate the tangent vectors in each component independently.

Tangential operations. For function $f : \mathbb{R}^d \rightarrow \mathbb{R}^{d'}$, the pseudo-hyperboloid version $f^\otimes : \mathcal{Q}_\beta^{s,t} \rightarrow \mathcal{Q}_\beta^{s',t'}$ with $s + t = d$ and $s' + t' = d'$ can be defined by the means of $\widehat{\log}_\mathbf{x}^\beta(\cdot)$ and $\widehat{\exp}_\mathbf{x}^\beta(\cdot)$ as Eq. (5).

$$f^\otimes(\cdot) := \widehat{\exp}_\mathbf{x}^\beta \left(f \left(\widehat{\log}_\mathbf{x}^\beta(\cdot) \right) \right), \quad (5)$$

where \mathbf{x} is the reference point. Note that this function is a morphism (i.e. $(f \circ g)^\otimes = f^\otimes \circ g^\otimes$) and direction preserving (i.e. $f^\otimes(\cdot)/\|f^\otimes(\cdot)\| = f(\cdot)/\|f(\cdot)\|$) [12], making it a natural way to define pseudo-hyperboloid version of vector operations such like scalar multiplication, matrix-vector multiplication, tangential aggregation and point-wise non-linearity and so on.

Parallel transport. Parallel transport is the generalization of Euclidean translation into manifolds. Formally, for any two points \mathbf{x} and \mathbf{y} connected by a geodesic, parallel transport $P_{\mathbf{x} \rightarrow \mathbf{y}}^\beta(\boldsymbol{\xi}) : \mathcal{T}_\mathbf{x} \mathcal{M} \rightarrow \mathcal{T}_\mathbf{y} \mathcal{M}$ is an isomorphism between two tangent spaces by moving one tangent vector $\boldsymbol{\xi} \in \mathcal{T}_\mathbf{x} \mathcal{M}$ with tangent direction $\boldsymbol{\xi} \in \mathcal{T}_\mathbf{x} \mathcal{M}$ to another tangent space $\mathcal{T}_\mathbf{y} \mathcal{M}$ (Cf. Fig. 2(b)). The parallel transport in pseudo-hyperboloid can be defined as the combination of Riemannian parallel transport [26], detailed in the Appendix C. However, the parallel transport has not been defined when there does not exist a geodesic between \mathbf{x} and \mathbf{y} . In other words, the tangent vector $\boldsymbol{\xi}$ induced by \mathbf{x} can not be transported to the tangent space of points outside of the normal neighborhood $\mathcal{U}_\mathbf{x}$. Intuitively, the normal neighborhoods satisfy the following property.

Theorem 3.7. *For any point $\mathbf{x} \in \mathcal{Q}_\beta^{s,t}$, the union of the normal neighborhood of \mathbf{x} and the normal neighborhood of its antipodal point $-\mathbf{x}$ cover the entire manifold. Namely, $\mathcal{U}_\mathbf{x} \cup \mathcal{U}_{-\mathbf{x}} = \mathcal{Q}_\beta^{s,t}$ (proof in Appendix E.7).*

This theorem ensures that if a point $\mathbf{y} \notin \mathcal{U}_{\mathbf{x}}$, its antipodal point $-\mathbf{y} \in \mathcal{U}_{\mathbf{x}}$. Besides, $\mathcal{T}_{\mathbf{y}}\mathcal{M}$ is parallel to $\mathcal{T}_{-\mathbf{y}}\mathcal{M}$. Hence, $P_{\mathbf{x} \rightarrow \mathbf{y}}^\beta$ can be alternatively defined as $P_{\mathbf{x} \rightarrow -\mathbf{y}}^\beta$ for broken points. This result is crucial to define the pseudo-hyperbolic addition, such as bias translation, detailed in section 4.

Geodesic distance. By the means of geodesic, the induced distance between \mathbf{x} and \mathbf{y} in pseudo-hyperboloid is defined as the arc length of geodesic $\gamma(\tau)$, given by $d_\gamma(\mathbf{x}, \mathbf{y}) = \sqrt{\|\log_{\mathbf{x}}(\mathbf{y})\|_t^2}$. For broken cases in which $\log_{\mathbf{x}}(\mathbf{y})$ is not defined, one approach is to use approximation like [19]. Different from that, we define following closed-form distance, given by Eq. (6).

$$D_\gamma(\mathbf{x}, \mathbf{y}) = \begin{cases} d_\gamma(\mathbf{x}, \mathbf{y}), & \text{if } \langle \mathbf{x}, \mathbf{y} \rangle_t < |\beta| \\ \pi\sqrt{|\beta|} + d_\gamma(\mathbf{x}, -\mathbf{y}), & \text{if } \langle \mathbf{x}, \mathbf{y} \rangle_t \geq |\beta| \end{cases} \quad (6)$$

The intuition is that when $\mathbf{x}, \mathbf{y} \in \mathcal{Q}_\beta^{s,t}$ are *g-disconnected*, we consider the distance as $d_\gamma(\mathbf{x}, \mathbf{y}) = d_\gamma(\mathbf{x}, -\mathbf{x}) + d_\gamma(-\mathbf{x}, \mathbf{y})$ or $d_\gamma(\mathbf{x}, \mathbf{y}) = d_\gamma(\mathbf{x}, -\mathbf{y}) + d_\gamma(-\mathbf{y}, \mathbf{y})$. Since $d_\gamma(\mathbf{x}, -\mathbf{x}) = d_\gamma(-\mathbf{y}, \mathbf{y}) = \pi\sqrt{|\beta|}$ is a constant and $d_\gamma(-\mathbf{x}, \mathbf{y}) = d_\gamma(\mathbf{x}, -\mathbf{y})$, the distance between broken points can be calculated as $d_\gamma(\mathbf{x}, \mathbf{y}) = \pi\sqrt{|\beta|} + d_\gamma(\mathbf{x}, -\mathbf{y})$. Fig. 2 (c) shows that the piecewise geodesic distance is defined on the combination of space-like, time-like and broken geodesics, which reflects the real distance more precisely than the approximation.

4 Semi-Riemannian GCNs

GCNs can be interpreted as performing neighborhood aggregation after a linear transformation on node features of each layer. We present semi-Riemannian GCNs (*Q*-GCN) by deriving corresponding operations with the developed geodesic tools in the pseudo-hyperboloid $\mathcal{Q}_\beta^{s,t}$.

Feature initialization. We first map the features from Euclidean space to pseudo-hyperboloid, considering that the input features of nodes usually live in Euclidean space. Following the feature transformation from Euclidean space to pseudo-hyperboloid in [19], we initialize the node features by performing a differentiable mapping $\varphi : \mathbb{R}_*^{t+1} \times \mathbb{R}^s \rightarrow \mathcal{Q}_\beta^{s,t}$ that can be composed of the diffeomorphisms from Theorem 3.2 or 3.3. The intuition is that we first map the Euclidean features into diffeomorphic manifolds $\mathbb{S}_{-\beta}^t \times \mathbb{R}^s$ (or $\mathbb{R}^{t-1} \times \mathbb{H}_\beta^{s+1}$) via $\psi(\cdot)$ and then map it into the pseudo-hyperboloid $\mathcal{Q}_\beta^{s,t}$ via $\psi^{-1}(\cdot)$, where the mapping functions are detailed in Appendix E.

Tangential transformation. We perform Euclidean transformations on the tangent space by leveraging the *expmap* and *logmap* defined in Eq. (3). Specifically, we first project the hidden feature into the tangent space of *south pole* $\mathbf{o} = [|\beta|, 0, \dots, 0]$ using *logmap* and then perform Euclidean matrix multiplication. Afterwards, the transformed features are mapped back to the manifold using *expmap*. Formally, at each layer ℓ , the tangential transformation is given by Eq. (7)

$$W^\ell \otimes^\beta \mathbf{h}^\ell := \widehat{\exp}_\mathbf{o}^\beta \left(W^\ell \widehat{\log}_\mathbf{o}^\beta (\mathbf{h}^\ell) \right), \quad (7)$$

where \otimes^β denotes the pseudo-hyperboloid tangential multiplication, $W^\ell \in \mathbb{R}^{d' \times d}$ denotes the layer-wise learnable matrix in Euclidean space.

Bias translation. To avoid model collapsing [27, 12], we perform bias translation after the tangential transformation. By the means of pseudo-hyperboloid *parallel transport*, the bias translation can be performed by parallel transporting a tangent vector $\mathbf{b}^\ell \in \mathcal{T}_\mathbf{o}\mathcal{Q}_\beta^{s,t}$ to the tangent space of the point of interest. Finally, the transported tangent vector is mapped back to the manifold with *expmap*. Considering that $\widehat{\exp}(\cdot)$ is only defined at point $\mathbf{x} \in \mathcal{Q}_\beta^{s,t}$ with the space dimension $\mathbf{x}_s = \mathbf{0}$, we perform the original $\exp_{\mathcal{Q}_\beta^{s,t}}(\cdot)$ at the point of interest. The bias translation is formally given by:

$$\tilde{\mathbf{h}}^\ell \oplus^\beta \mathbf{b}^\ell := \begin{cases} \exp_{\tilde{\mathbf{h}}^\ell}^\beta \left(P_{\mathbf{o} \rightarrow \tilde{\mathbf{h}}^\ell}^\beta (\mathbf{b}^\ell) \right), & \text{if } \langle \mathbf{o}, \tilde{\mathbf{h}}^\ell \rangle_t < |\beta| \\ -\exp_{-\tilde{\mathbf{h}}^\ell}^\beta \left(P_{\mathbf{o} \rightarrow -\tilde{\mathbf{h}}^\ell}^\beta (\mathbf{b}^\ell) \right), & \text{if } \langle \mathbf{o}, \tilde{\mathbf{h}}^\ell \rangle_t \geq |\beta| \end{cases} \quad (8)$$

where $\tilde{\mathbf{h}}^\ell$ denotes $W^\ell \otimes^\beta \mathbf{h}^\ell$, \oplus^β denotes the pseudo-hyperboloid addition. For the broken cases where $\langle \mathbf{o}, \tilde{\mathbf{h}}^\ell \rangle_t \geq |\beta|$, the parallel transport $P_{\mathbf{o} \rightarrow \tilde{\mathbf{h}}^\ell}^\beta$ is not defined. In this case, we parallel transport \mathbf{b}^ℓ to the tangent space of the antipodal point $-\tilde{\mathbf{h}}^\ell$, and then perform $\exp_{-\tilde{\mathbf{h}}^\ell}^\beta$ to map it back to the

Table 1: The graph reconstruction results in mAP (%), top three results are highlighted.

Model	Web-Edu	Power	Bio-Worm	Facebook
Sectional curvature	-0.6	-0.3	0.0	0.1
GCN (\mathbb{E}^{10}) [2]	83.66	86.61	90.19	81.73
HGCN (\mathbb{H}^{10}) [27]	88.33	93.80	93.12	83.40
GCN (\mathbb{S}^{10}) [28]	82.72	92.73	88.98	81.04
Prod-GCN ($\mathbb{H}^5 \times \mathbb{H}^5$)	89.21	94.40	94.00	84.94
Prod-GCN ($\mathbb{S}^5 \times \mathbb{S}^5$)	86.70	94.58	90.36	84.56
Prod-GCN ($\mathbb{H}^5 \times \mathbb{S}^5$)	87.96	95.82	94.74	87.73
\mathcal{Q} -GCN ($\mathcal{Q}^{9,1}$)	87.03	94.35	92.83	81.60
\mathcal{Q} -GCN ($\mathcal{Q}^{7,3}$)	99.67	100.00	97.23	87.74
\mathcal{Q} -GCN ($\mathcal{Q}^{5,5}$)	98.49	100.00	95.75	87.03
\mathcal{Q} -GCN ($\mathcal{Q}^{3,7}$)	97.31	95.08	90.14	91.75
\mathcal{Q} -GCN ($\mathcal{Q}^{0,10}$)	82.57	94.20	88.67	83.81

manifold. Note that the images of $\exp_{\tilde{\mathbf{h}}^\ell}^\beta$ and $\exp_{-\tilde{\mathbf{h}}^\ell}^\beta$ cover the entire manifold, a point $\tilde{\mathbf{h}}^\ell \in \mathcal{Q}^{s,t}$ can therefore be translated into any position of $\mathcal{Q}_\beta^{s,t}$.

Tangential Aggregation. The linear combination of neighborhood features is lifted to the tangent space, which is an intrinsic operation in differential manifolds [27, 13]. Specifically, \mathcal{Q} -GCN aggregates neighbours’ embeddings in the tangent space of the reference point \mathbf{o} before passing through a tangential activation function, and then projects the updated representation back to the manifold. Formally, at each layer ℓ , the updated features of each node i are defined as Eq. (9).

$$\mathbf{h}_i^{\ell+1} = \widehat{\exp}_{\mathbf{o}}^{\beta_{\ell+1}} \left(\sigma \left(\sum_{j \in \mathcal{N}(i) \cup \{i\}} \widehat{\log}_{\mathbf{o}}^{\beta_\ell} \left(W^\ell \otimes^{\beta_\ell} \mathbf{h}_j^\ell \oplus^{\beta_\ell} \mathbf{b}^\ell \right) \right) \right), \quad (9)$$

where $\sigma(\cdot)$ is the activation function, β_ℓ and $\beta_{\ell+1}$ are two layer-wise trainable curvatures, $\mathcal{N}(i)$ denotes the one-hop neighborhoods of node i . We generalize the layer-wise trainable curvature in hyperbolic space [27] to pseudo-hyperboloid, to capture the right scale of embeddings at each layer, detailed in Appendix F.2. The pseudo-hyperboloid embeddings at the last layer can then be used for downstream tasks such as predicting node attributes or links.

5 Experiments

In this section, we comprehensively evaluate the effectiveness of \mathcal{Q} -GCN on graph reconstruction, node classification and link prediction. We first study the geometric properties of the used graphs including the graph sectional curvature [16] and the δ -hyperbolicity [7], detailed in the Appendix G.1.

5.1 Graph Reconstruction

For graph reconstruction, the objective is to map all nodes into a low-dimensional space such that the connected nodes are closer than unconnected nodes. Following [16, 19], we minimize the loss function $\mathcal{L}(\Theta) = \sum_{(u,v) \in \mathcal{D}} \log \frac{e^{-d(\mathbf{u}, \mathbf{v})}}{\sum_{v' \in \mathcal{E}(u)} e^{-d(\mathbf{u}, \mathbf{v}')}}}$ under the set of connected relations \mathcal{D} in the graph, where $\mathcal{E}(u) = \{v | (u, v) \notin \mathcal{D}, v \neq u\}$ is the set of negative examples for node u , $d(\cdot)$ is the distance function defined in Eq. (6). We report the mean average precision (mAP) for evaluation [16]. See Appendix G.2 for details of the task.

Datasets and Baselines. We benchmark graph reconstruction on four real-world graphs including 1) Web-Edu [29]: a web network consisting of the .edu domain; 2) Power [30]: a power grid distribution network with backbone structure; 3) Bio-Worm [31]: a worms gene network; 4) Facebook [32]: a dense social network from Facebook. We compare our method with Euclidean GCN [2], HGCN [27], spherical GCN, and Prod-GCN [28] with three variants. Besides, five variants of our model are implemented with different time dimension in [1, 3, 5, 7, 10] for comparison.

Experimental Settings. Following [16, 19, 28], we use one-hot embeddings as initial node features. To avoid the time dimensions be 0, we uniformly perturb each dimension with a small random value

Table 2: ROC AUC for Link Prediction (LP) and F1 score for Node Classification (NC) (%).

Dataset δ -hyperbolicity	Airport 1.0		Pubmed 3.5		CiteSeer 4.5		Cora 11.0	
Method	LP	NC	LP	NC	LP	NC	LP	NC
GCN [2]	89.24 \pm 0.21	81.54 \pm 0.60	91.31 \pm 1.68	79.30 \pm 0.60	85.48 \pm 1.75	72.27 \pm 0.64	88.52 \pm 0.85	81.90 \pm 0.41
GAT [3]	90.35 \pm 0.30	81.55 \pm 0.53	87.45 \pm 0.00	78.30 \pm 0.00	87.24 \pm 0.00	71.10 \pm 0.00	85.73 \pm 0.01	83.05 \pm 0.08
SAGE [33]	89.86 \pm 0.52	82.79 \pm 0.17	90.70 \pm 0.07	77.30 \pm 0.09	90.71 \pm 0.20	69.20 \pm 0.10	87.52 \pm 0.22	74.90 \pm 0.07
SGC [4]	89.80 \pm 0.34	80.69 \pm 0.23	90.54 \pm 0.07	78.60 \pm 0.30	89.61 \pm 0.23	71.60 \pm 0.03	89.42 \pm 0.11	81.60 \pm 0.43
HGCN [27] (\mathbb{H}^{16})	96.03\pm0.26	90.57\pm0.36	96.08\pm0.21	80.50\pm1.23	96.31\pm0.41	68.90 \pm 0.63	91.62 \pm 0.33	79.90 \pm 0.18
κ -GCN [28] (\mathbb{H}^{16})	96.35\pm0.62	87.92\pm1.33	96.60 \pm 0.32	77.96 \pm 0.36	95.34 \pm 0.16	73.25\pm0.51	94.04 \pm 0.34	79.80 \pm 0.50
κ -GCN [28] (\mathbb{S}^{16})	90.38 \pm 0.32	81.94 \pm 0.58	94.84 \pm 0.13	78.80 \pm 0.49	95.79 \pm 0.24	72.13 \pm 0.51	93.20 \pm 0.48	81.08 \pm 1.45
κ -GCN [28] ($\mathbb{H}^8 \times \mathbb{S}^8$)	93.10 \pm 0.49	81.93 \pm 0.45	94.89 \pm 0.19	79.20 \pm 0.65	93.44 \pm 0.31	73.05 \pm 0.59	92.22 \pm 0.48	79.30 \pm 0.81
\mathcal{Q} -GCN ($\mathcal{Q}^{15,1}$)	96.30\pm0.22	89.72\pm0.52	95.42 \pm 0.22	80.50\pm0.26	94.76 \pm 1.49	72.67 \pm 0.76	93.14 \pm 0.30	80.57 \pm 0.20
\mathcal{Q} -GCN ($\mathcal{Q}^{14,2}$)	94.37 \pm 0.44	84.40 \pm 0.35	96.86\pm0.37	81.34\pm1.54	94.78 \pm 0.17	73.43\pm0.58	93.41 \pm 0.57	81.62 \pm 0.21
\mathcal{Q} -GCN ($\mathcal{Q}^{13,3}$)	92.53 \pm 0.17	82.38 \pm 1.53	96.20\pm0.34	80.94\pm0.45	94.54 \pm 0.16	74.13\pm1.41	93.56 \pm 0.18	79.91 \pm 0.42
\mathcal{Q} -GCN ($\mathcal{Q}^{2,14}$)	90.03 \pm 0.12	81.14 \pm 1.32	94.30 \pm 1.09	78.40 \pm 0.39	94.80 \pm 0.08	72.72 \pm 0.47	94.17\pm0.38	83.10\pm0.35
\mathcal{Q} -GCN ($\mathcal{Q}^{1,15}$)	89.07 \pm 0.58	81.24 \pm 0.34	94.66 \pm 0.18	78.11 \pm 1.38	97.01\pm0.30	73.19\pm1.58	94.81\pm0.27	83.72\pm0.43
\mathcal{Q} -GCN ($\mathcal{Q}^{0,16}$)	89.01 \pm 0.61	80.91 \pm 0.65	94.49 \pm 0.28	77.90 \pm 0.80	96.21\pm0.38	72.54 \pm 0.27	95.16\pm1.25	82.51 \pm 0.32

in the interval $[-\epsilon, \epsilon]$, where $\epsilon = 0.02$ in practice. In addition, the same 10-dimensional embedding and 2 hidden layers are used for all baselines to ensure a fair comparison. The learning rate is set to 0.01, the learning rate of curvature is set to 0.0001. \mathcal{Q} -GCN is implemented with the Adam optimizer. We repeat the experiments 5 times via random seeds and report the mean results.

Results. Table 1 shows the results of graph reconstruction on four datasets. It shows that \mathcal{Q} -GCN achieves the best performance across all benchmarks compared with both Riemannian space and product manifolds. We observe that by setting proper signatures, the product spaces perform better than a single geometry. It is consistent with our statement that the expression power of a single view geometry is limited. Specifically, all the top three results are achieved by \mathcal{Q} -GCN, with one exception on Power where $\mathbb{H}^5 \times \mathbb{S}^5$ achieved the third best performance. More precisely, for datasets that have smaller graph sectional curvature like Web-Edu, Power and Bio-Worm, $\mathcal{Q}^{7,3}$ perform the best, while $\mathcal{Q}^{3,7}$ perform the best on Facebook with positive sectional curvature. We conjecture that the number of time dimensions control the geometry of the pseudo-hyperboloid, analysed in Section 5.3.

5.2 Node Classification and Link Prediction

For node classification, we map the output of the last layer of \mathcal{Q} -GCN to the tangent space, and then perform Euclidean multinomial logistic regression. For link prediction, we utilize the Fermi-Dirac decoder [8] to compute probability scores for edges, and then train \mathcal{Q} -GCN by minimizing the cross-entropy loss using negative sampling.

Datasets and Baselines. We consider four real-world benchmark datasets: Airport, Pubmed, Citeseer and Cora, where Airport is airline networks, Pubmed, Citeseer and Cora are three citation networks. GCN [2], GAT [3], SAGE [33] and SGC [4] are used as Euclidean counterparts. For non-Euclidean baselines, we compare HGCN [27] and κ -GCN [28] with its three variants. For \mathcal{Q} -GCN, we set time dimension in $[1, 2, 3, 14, 15, 16]$ as six variants.

Experimental Settings. For node classification, we use the same dataset split as [34] for citation datasets, where 20 nodes per class are used for training, and 500 nodes used for validation and 1000 nodes used for testing. For Airport, we split the dataset into 70/15/15. For link prediction, the edges are split into 85/5/10 percent for training, validation and testing for all datasets. To ensure a fair comparison, we set the same 16-dimension hidden embedding, 0.01 initial learning rate and 0.0001 learning rate for curvature. The optimal regularization with weight decay, dropout rate, the number of layers and activation functions are obtained by grid search for each method. We report the mean accuracy over 10 random seed initializations. See Appendix G.4 for more details.

Results. Table 2 shows the averaged ROC AUC for link prediction, and F1 score for node classification. We observe that the graph sectional curvatures of the four datasets are consistently negative without significant differences, hence we report the additional δ -hyperbolicity for analysis. For Airport and Pubmed with dominating hierarchical properties (lower δ), \mathcal{Q} -GCNs with lower time dimensions achieve the results on par with hyperbolic space based methods such as HGCN [27], κ -GCN (\mathbb{H}^{16}). While for CiteSeer and Cora with less tree-like properties (higher δ), \mathcal{Q} -GCNs achieve the state-of-the-art results, showcasing the flexibility of our model to embed complex graphs with different curvatures.

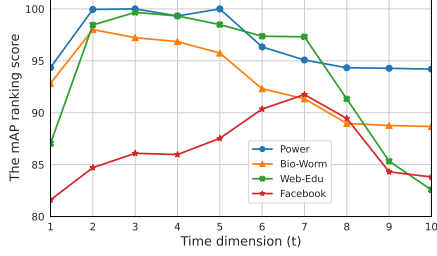


Figure 3: The mAP of graph reconstruction with varying number of time dimensions.

Method	Pubmed	CiteSeer	Cora
MLP	72.30±0.30	60.22±0.42	55.80±0.08
HNN	74.60±0.40	59.92±0.87	59.60±0.09
Q -NN ($Q^{15,1}$)	74.31±0.33	59.33±0.35	60.38±0.56
Q -NN ($Q^{14,2}$)	76.26±0.31	64.33±0.35	62.77±0.30
Q -NN ($Q^{13,3}$)	75.85±0.79	63.65±0.57	59.04±0.45
Q -NN ($Q^{2,14}$)	74.44±0.68	60.48±0.29	63.85±0.22
Q -NN ($Q^{1,15}$)	73.44±0.28	60.33±0.40	64.85±0.24
Q -NN ($Q^{0,16}$)	73.31±0.17	61.05±0.22	63.96±0.41

Table 3: F1 score for node classification of MLP, HNN and Q -NN on Pubmed, Citeseer and Cora.

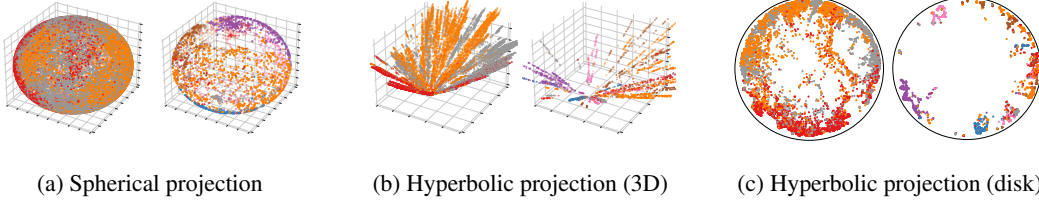


Figure 4: Visualization of embeddings for link prediction on Pubmed (left) and Cora (right), where the colors denote the class of nodes. We apply (a) spherical projection, (b) hyperbolic projection (3D) and (c) hyperbolic projection (Poincaré disk) on the learned embeddings of Q -GCN to visualize the various views of the learned embeddings.

5.3 Analysis

Ablation study of time dimension. We study the influence of time dimension for graph reconstruction by setting varying number of time dimensions under the condition of $s + t = 10$. Fig. 3 shows that the *time dimension* t acts as a knob for controlling the geometric properties of $Q_{\beta}^{s,t}$. As can be seen, the best performance are achieved by neither hyperboloid ($t = 1$) nor sphere cases ($t = 10$), showcasing the advantages of $Q_{\beta}^{s,t}$ on representing graphs of mixed topologies. It shows that on Web-Edu, Power and Bio-Worm with smaller (non-positive) mean sectional curvature, after the optimal value is reached at a lower t , the performance decrease as t increases. While on Facebook with larger (positive) mean sectional curvature, as t rises, the effect gradually increases until it reaches a peak at a higher t . It is consistent with our hypothesis that graphs with more hierarchical structure are inclined to be embedded in $Q_{\beta}^{s,t}$ with smaller t , while cyclical data is aligned well with larger t . The results give us an intuition to determine the best time dimension based on the geometric properties of graphs.

Q -NN VS Q -GCN. We also introduce Q -NN, a generalization of MLP into semi-Riemannian manifold, defined as multiple layers of $f(\mathbf{x}) = \sigma^{\otimes}(W \otimes^{\beta} \mathbf{x} \oplus^{\beta} \mathbf{b})$, where σ^{\otimes} is the tangential activation. Table 3 shows that Q -NN with appropriate time dimension outperforms MLP and HNN on node classification, showcasing the expression power of pseudo-hyperboloid. Furthermore, compared with the results of Q -GCN in Table 2, Q -GCN performs better than Q -NN, suggesting that the benefits of the neighborhood aggregation equipped with the proposed graph convolutional operations.

Visualization. To visualize the embeddings learned by Q -GCN, we conduct three projections of different geometric views that decompose the learned embeddings for Link Prediction on Pubmed and Cora, including spherical projection into 3D sphere, hyperbolic projection into 3D plane and 2D Poincaré disk. As shown in Fig. 4 (a,b), for Pubmed with more hyperbolic structures, the class separability is more significant in hyperbolic projection than it is in spherical projection. While the corresponding result is opposite for less tree-like Cora. Furthermore, Fig. 4 (c) provides a more clear insight of the hierarchy. It shows that there are more hub nodes near the origin of Poincaré disk in Pubmed than in Cora, showcasing the dominating tree-likeness of Pubmed.

6 Conclusion

In this paper, we generalize GCNs in a principled manner to semi-Riemannian manifolds of constant nonzero curvature with the elegant theory of diffeomorphic geometry tools. The proposed semi-

Riemannian GCNs have the flexibility to fit well the complex graphs with mixed curvatures and have shown promising results on graph reconstruction, node classification and link prediction tasks. The developed geodesic tools are application agnostic and could be extended to more deep learning methods. We foresee our work will open a new direction for non-Euclidean geometric deep learning.

Broader Impact

Going beyond Riemannian manifolds, we extend GCNs to the semi-Riemannian manifolds, which is a smooth manifold furnished with indefinite metric. Our contribution is both theoretical and practical. We introduce necessary geodesic tools in geodesically disconnected semi-Riemannian manifolds to help machine learning researchers to define vector operations like matrix multiplication and vector addition. These operations are application agnostic and could be applied in the context of machine learning algorithms. \mathcal{Q} -GCN is a flexible framework and is especially powerful on modeling real-world graphs such as social networks and molecular networks which usually exhibit heterogeneous topological structures. We foresee our method can be applied to more practical settings such as recommender systems and drug discovery, and also stimulate more applications of semi-Riemannian geometry in machine learning and related communities.

However, we emphasize that current models might suffer from the same problems as other deep models such as limited interpretability, and thus, are not capable of replacing human expertise. We advocate researchers to focus more on the interpretability of non-Euclidean graph embeddings.

Acknowledgments

The authors thank the International Max Planck Research School for Intelligent Systems (IMPRS-IS) for supporting Bo Xiong. This project has received funding from the European Union’s Horizon 2020 research and innovation programme under the Marie Skłodowska-Curie grant agreement No: 860801.

References

- [1] Joan Bruna, Wojciech Zaremba, Arthur Szlam, and Yann LeCun. Spectral networks and locally connected networks on graphs. In *Proceedings of the International Conference on Learning Representations*, 2014.
- [2] Thomas N. Kipf and Max Welling. Semi-supervised classification with graph convolutional networks. In *5th International Conference on Learning Representations, ICLR 2017, Toulon, France, April 24-26, 2017, Conference Track Proceedings*. OpenReview.net, 2017.
- [3] Petar Velickovic, Guillem Cucurull, Arantxa Casanova, Adriana Romero, Pietro Liò, and Yoshua Bengio. Graph attention networks. In *6th International Conference on Learning Representations, ICLR 2018, Vancouver, BC, Canada, April 30 - May 3, 2018, Conference Track Proceedings*. OpenReview.net, 2018.
- [4] Felix Wu, Amauri H. Souza Jr., Tianyi Zhang, Christopher Fifty, Tao Yu, and Kilian Q. Weinberger. Simplifying graph convolutional networks. In *Proceedings of the International Conference on Machine Learning*, volume 97 of *Proceedings of Machine Learning Research*, pages 6861–6871. PMLR, 2019.
- [5] Ke Sun, Jun Wang, Alexandros Kalousis, and Stéphane Marchand-Maillet. Space-time local embeddings. In *Advances in Neural Information Processing Systems*, pages 100–108, 2015.
- [6] Marián Boguñá, Ivan Bonamassa, Manlio De Domenico, Shlomo Havlin, Dmitri Krioukov, and M Ángeles Serrano. Network geometry. *Nature Reviews Physics*, pages 1–22, 2021.
- [7] Mikhael Gromov. Hyperbolic groups. In *Essays in group theory*, pages 75–263. Springer, 1987.
- [8] Dmitri Krioukov, Fragiskos Papadopoulos, Maksim Kitsak, Amin Vahdat, and Marián Boguñá. Hyperbolic geometry of complex networks. *Physical Review E*, 82(3):036106, 2010.
- [9] Richard C Wilson, Edwin R Hancock, Elżbieta Pekalska, and Robert PW Duin. Spherical and hyperbolic embeddings of data. *IEEE transactions on pattern analysis and machine intelligence*, 36(11):2255–2269, 2014.

- [10] Yu Meng, Jiaxin Huang, Guangyuan Wang, Chao Zhang, Honglei Zhuang, Lance M. Kaplan, and Jiawei Han. Spherical text embedding. In *Advances in Neural Information Processing Systems*, pages 8206–8215, 2019.
- [11] Michaël Defferrard, Nathanaël Perraudin, Tomasz Kacprzak, and Raphael Sgier. Deepsphere: towards an equivariant graph-based spherical cnn. *arXiv preprint arXiv:1904.05146*, 2019.
- [12] Octavian-Eugen Ganea, Gary Bécigneul, and Thomas Hofmann. Hyperbolic neural networks. In *Advances in neural information processing systems*, pages 5350–5360, 2018.
- [13] Qi Liu, Maximilian Nickel, and Douwe Kiela. Hyperbolic graph neural networks. In *Advances in Neural Information Processing Systems*, pages 8228–8239, 2019.
- [14] Shichao Zhu, Shirui Pan, Chuan Zhou, Jia Wu, Yanan Cao, and Bin Wang. Graph geometry interaction learning. In *Advances in Neural Information Processing Systems*, 2020.
- [15] Yiding Zhang, Xiao Wang, Chuan Shi, Nian Liu, and Guojie Song. Lorentzian graph convolutional networks. In *International World Wide Web Conference Committee*, 2021.
- [16] Albert Gu, Frederic Sala, Beliz Gunel, and Christopher Ré. Learning mixed-curvature representations in product spaces. In *7th International Conference on Learning Representations, ICLR 2019, New Orleans, LA, USA, May 6-9, 2019*. OpenReview.net, 2019.
- [17] Ondrej Skopek, Octavian-Eugen Ganea, and Gary Bécigneul. Mixed-curvature variational autoencoders. In *8th International Conference on Learning Representations, ICLR 2020, Addis Ababa, Ethiopia, April 26-30, 2020*. OpenReview.net, 2020.
- [18] Julian Laub and Klaus-Robert Müller. Feature discovery in non-metric pairwise data. *The Journal of Machine Learning Research*, 5:801–818, 2004.
- [19] Marc T. Law and Jos Stam. Ultrahyperbolic representation learning. In *Advances in neural information processing systems*, 2020.
- [20] Barrett O’neill. Semi-riemannian geometry with applications to relativity. *Academic press*, 103, 1983.
- [21] H Anciaux. Minimal submanifolds in pseudo-riemannian geometry. *World Scientific*, 2011.
- [22] Barrett O’neill. *Semi-Riemannian geometry with applications to relativity*. Academic press, 1983.
- [23] Daniel Spiegel. The hopf-rinow theorem. *Notes available online*, 2016.
- [24] Miguel Sánchez. Geodesic connectedness of semi-riemannian manifolds. *arXiv preprint math/0005039*, 2000.
- [25] Fabio Giannoni, Paolo Piccione, and Rosella Sampalmieri. On the geodesical connectedness for a class of semi-riemannian manifolds. *Journal of mathematical analysis and applications*, 252(1):444–476, 2000.
- [26] Tingran Gao, Lek-Heng Lim, and Ke Ye. Semi-riemannian manifold optimization. *arXiv preprint arXiv:1812.07643*, 2018.
- [27] Ines Chami, Zhitaoying, Christopher Ré, and Jure Leskovec. Hyperbolic graph convolutional neural networks. In *Advances in neural information processing systems*, pages 4869–4880, 2019.
- [28] Gregor Bachmann, Gary Bécigneul, and Octavian Ganea. Constant curvature graph convolutional networks. In *Proceedings of the 37th International Conference on Machine Learning, ICML 2020, 13-18 July 2020, Virtual Event*, volume 119 of *Proceedings of Machine Learning Research*, pages 486–496. PMLR, 2020.
- [29] David Gleich, Leonid Zhukov, and Pavel Berkhin. Fast parallel pagerank: A linear system approach. *Yahoo! Research Technical Report YRL-2004-038*, available via <http://research.yahoo.com/publication/YRL-2004-038.pdf>, 13:22, 2004.
- [30] Duncan J Watts and Steven H Strogatz. Collective dynamics of ‘small-world’ networks. *nature*, 393(6684):440–442, 1998.
- [31] Ara Cho, Junha Shin, Sohyun Hwang, Chanyoung Kim, Hongseok Shim, Hyojin Kim, Han-hae Kim, and Insuk Lee. Wormnet v3: a network-assisted hypothesis-generating server for caenorhabditis elegans. *Nucleic acids research*, 42(W1):W76–W82, 2014.

- [32] Julian J. McAuley and Jure Leskovec. Learning to discover social circles in ego networks. In *Advances in Neural Information Processing Systems*, pages 548–556, 2012.
- [33] William L. Hamilton, Zhitao Ying, and Jure Leskovec. Inductive representation learning on large graphs. In *Advances in neural information processing systems*, pages 1024–1034, 2017.
- [34] Zhilin Yang, William W. Cohen, and Ruslan Salakhutdinov. Revisiting semi-supervised learning with graph embeddings. In *Proceedings of the International Conference on Machine Learning*, volume 48 of *JMLR Workshop and Conference Proceedings*, pages 40–48. JMLR.org, 2016.
- [35] Maximilian Nickel and Douwe Kiela. Poincaré embeddings for learning hierarchical representations. *arXiv preprint arXiv:1705.08039*, 2017.
- [36] Bhuwan Dhingra, Christopher Shallue, Mohammad Norouzi, Andrew Dai, and George Dahl. Embedding text in hyperbolic spaces. In *Proceedings of the Twelfth Workshop on Graph-Based Methods for Natural Language Processing (TextGraphs-12)*, pages 59–69, New Orleans, Louisiana, USA, 2018. Association for Computational Linguistics.
- [37] Ivana Balazevic, Carl Allen, and Timothy M. Hospedales. Multi-relational poincaré graph embeddings. In *Advances in neural information processing systems*, pages 4465–4475, 2019.
- [38] Tim R. Davidson, Luca Falorsi, Nicola De Cao, Thomas Kipf, and Jakub M. Tomczak. Hyperspherical variational auto-encoders. In *Proceedings of the Thirty-Fourth Conference on Uncertainty in Artificial Intelligence*, pages 856–865. AUAI Press, 2018.
- [39] Jiacheng Xu and Greg Durrett. Spherical latent spaces for stable variational autoencoders. In *Proceedings of the 2018 Conference on Empirical Methods in Natural Language Processing*, pages 4503–4513, Brussels, Belgium, 2018. Association for Computational Linguistics.
- [40] Zhen Han, Peng Chen, Yunpu Ma, and Volker Tresp. DyERNIE: Dynamic Evolution of Riemannian Manifold Embeddings for Temporal Knowledge Graph Completion. In *Proceedings of the 2020 Conference on Empirical Methods in Natural Language Processing (EMNLP)*, pages 7301–7316, Online, 2020. Association for Computational Linguistics.
- [41] John M Lee. Smooth manifolds. In *Introduction to Smooth Manifolds*, pages 1–31. Springer, 2013.
- [42] Peter Petersen, S Axler, and KA Ribet. *Riemannian geometry*, volume 171. Springer, 2006.
- [43] Thomas James Willmore. *An introduction to differential geometry*. Courier Corporation, 2013.
- [44] Keyulu Xu, Chengtao Li, Yonglong Tian, Tomohiro Sonobe, Ken-ichi Kawarabayashi, and Stefanie Jegelka. Representation learning on graphs with jumping knowledge networks. In *International Conference on Machine Learning*, pages 5453–5462. PMLR, 2018.
- [45] Ming Chen, Zhewei Wei, Zengfeng Huang, Bolin Ding, and Yaliang Li. Simple and deep graph convolutional networks. In *International Conference on Machine Learning*, pages 1725–1735. PMLR, 2020.
- [46] Yulong Pei, Tianjin Huang, Werner van Ipenburg, and Mykola Pechenizkiy. Resgcn: Attention-based deep residual modeling for anomaly detection on attributed networks. *arXiv preprint arXiv:2009.14738*, 2020.

Appendices

Supplemental Material of "Semi-Riemannian Graph Convolution Networks"

We structurize our supplementary materials as follows:

- Sec. A summarizes the frequently used notations and the conventions.
- Sec. B reviews some related works on Riemannian embeddings and the application of semi-Riemannian geometry in machine learning.
- Sec. C reviews semi-Riemannian geometry and provides some standard geodesic tools in pseudo-hyperboloid.
- Sec. D reviews some relevant concepts of Riemannian geometry.
- Sec. E provides necessary proofs of the theorems mentioned in the paper.
- Sec. F provides additional theorems mentioned in the paper.
- Sec. G provides more details about the experimental setup and analysis.

A Notation

In this paper, we denote the points on manifolds by boldface Roman characters. The tangent vectors on tangent spaces are denoted by boldface Greek fonts. The notations are summarized in Table 4.

Table 4: Commonly used notations.

Notations	Descriptions
$\mathcal{Q}_\beta^{s,t}$	A pseudo-hyperboloid with s space dimensions and t time dimensions
$\mathbf{x}, \mathbf{y}, \mathbf{z}$	The points in manifolds
$\boldsymbol{\xi}, \boldsymbol{\zeta}$	The tangent vectors in tangent space
$\mathcal{T}_x \mathcal{M}$	The tangent space at point $\mathbf{x} \in \mathcal{M}$
\mathbb{R}	A Euclidean space
\mathbb{R}_*	The Euclidean space excluded point $\mathbf{0} = [0, 0, \dots, 0]$
\mathbb{S}	A spherical space
\mathbb{H}	A hyperbolic space
\mathcal{U}_x	The normal neighborhood of point \mathbf{x}
$\gamma_{\mathbf{x} \rightarrow \boldsymbol{\xi}}(\tau)$	The geodesic of mapping a real value τ to a point on \mathcal{M} with tangent direction $\boldsymbol{\xi} \in \mathcal{T}_x \mathcal{M}$
\exp	The exponential map
\log	The logarithmic map
$\widehat{\exp}$	The diffeomorphic exponential map
$\widehat{\log}$	The diffeomorphic logarithmic map
$P_{\mathbf{x} \rightarrow \mathbf{y}}^\beta(\boldsymbol{\xi})$	The parallel transport of one tangent vector on $\mathcal{T}_x \mathcal{M}$ with tangent direction $\boldsymbol{\xi} \in \mathcal{T}_x \mathcal{M}$ to another tangent space $\mathcal{T}_y \mathcal{M}$
β	The curvature parameter of pseudo-hyperboloid
K	The curvature of Riemannian manifolds
ψ	The diffeomorphic function
$\psi_{\mathbb{S}}, \psi_{\mathbb{H}}$	The spherical diffeomorphic function and hyperbolic diffeomorphic function
$d_\gamma(\mathbf{x}, \mathbf{y})$	The distance between points \mathbf{x} and \mathbf{y}
\otimes^β	Pseudo-hyperboloid multiplication
\oplus^β	Pseudo-hyperboloid addition

B Related Works

Riemannian Embeddings. Non-Euclidean Riemannian spaces have recently gained extensive attention in learning representation for non-euclidean data wilson2014spherical. [35] was the first

work to learn hierarchical embedding in hyperbolic space for link prediction. Following this work, [36] applied hyperbolic embedding in word embedding. [37] proposed a translation model in hyperbolic space for multi-relational graph embedding. On the other hand, spherical space offers benefits for embedding spherical or cyclical data [11, 38, 39]. For mixed curvature space, product manifolds [16, 17] on Euclidean, hyperbolic and spherical space has been proposed to embed graph and knowledge graphs [40] with mixed structures. HNN [12] firstly extended neural networks into the hyperbolic space and defined some fundamental neural operations.

Riemannian GCNs. Going beyond GCNs in Euclidean space [1, 2], HGNN [13] and HGCN [27] first extended GCNs into hyperbolic space, achieving state-of-the-art performance on learning graph embedding for scale-free networks. The main solution is to move the graph convolutional operations (e.g. *feature transformation, aggregation*) into the *tangent space* of manifolds and perform Euclidean operations on the space. To model graphs of mixed topologies, κ -GCN [28] unifies curvatures in a κ -stereographic model and extends GCNs into the products of Riemannian projection manifolds. GIL [14] proposed graph geometric interaction learning that model interaction between hyperbolic and Euclidean space. Different from these works, \mathcal{Q} -GCN learns graph embeddings in a single semi-Riemannian space with indefinite metric while captures mixed graph structures.

Machine Learning with Semi-Riemannian Geometry. Few works [5, 26, 19] have explored the application of semi-Riemannian geometry in machine learning. [5] first apply semi-Riemannian geometry (or *pseudo-Euclidean space*) to embed non-metric data that preserves local information. [26] developed a manifold learning framework on semi-Riemannian manifold and its submanifolds. More recently, [19] proposed learning graph embeddings on pseudo-hyperboloid and provided some necessary geodesic tools. However, semi-Riemannian geometry has not yet been studied in the setting of deep learning.

C Review of Semi-Riemannian Geometry

We review some basic notions of semi-Riemannian manifolds and the geodesic tools of pseudo-hyperboloid.

C.1 Semi-Riemannian Manifold

The semi-Riemannian (or pseudo-Riemannian) manifold \mathcal{M} is equipped with a semi-Riemannian metric $g_{\mathbf{x}} : \mathcal{T}_{\mathbf{x}}\mathcal{M} \times \mathcal{T}_{\mathbf{x}}\mathcal{M}$ at point \mathbf{x} . The metric $g_{\mathbf{x}}$ is a nondegenerate symmetric bilinear form, which means that if for a given $\xi \in \mathcal{T}_{\mathbf{x}}\mathcal{M}$, for any $\zeta \in \mathcal{T}_{\mathbf{x}}\mathcal{M}$ we have $g_{\mathbf{x}}(\xi, \zeta) = 0$, then $\xi = \mathbf{0}$. The \mathcal{M} manifold has the constant sectional curvature of $1/\beta$ and constant mean curvature $\kappa = |\beta|^{-1/2}$. The standard book [21] contains a detailed description.

C.2 Geodesic Tools of pseudo-hyperboloid

Although pseudo-hyperboloid is a *geodesically disconnected* manifold, previous works [19, 26] have defined some standard geodesic tools that do not consider the broken cases which we recall below.

Geodesic. The geodesics of pseudo-hyperboloid are a combination of the hyperbolic, flat and spherical cases, depending on the sign of $\langle \xi, \xi \rangle_t$. Formally, the geodesic $\gamma_{\mathbf{x} \rightarrow \xi}(\tau)$ of $\mathcal{Q}_{\beta}^{s,t}$ with $\beta < 0$ is defined as Eq. (10).

$$\gamma_{\mathbf{x} \rightarrow \xi}(\tau) = \begin{cases} \cosh\left(\frac{\tau\sqrt{|\langle \xi, \xi \rangle_t|}}{\sqrt{|\beta|}}\right) \mathbf{x} + \frac{\sqrt{|\beta|}}{\sqrt{\langle \xi, \xi \rangle_t}} \sinh\left(\frac{\tau\sqrt{|\langle \xi, \xi \rangle_t|}}{\sqrt{|\beta|}}\right), & \text{if } \langle \xi, \xi \rangle_t > 0 \\ \mathbf{x} + \tau\xi, & \text{if } \langle \xi, \xi \rangle_t = 0 \\ \cos\left(\frac{\tau\sqrt{|\langle \xi, \xi \rangle_t|}}{\sqrt{|\beta|}}\right) \mathbf{x} + \frac{\sqrt{|\beta|}}{\sqrt{\langle \xi, \xi \rangle_t}} \sin\left(\frac{\tau\sqrt{|\langle \xi, \xi \rangle_t|}}{\sqrt{|\beta|}}\right) \xi, & \text{if } \langle \xi, \xi \rangle_t < 0 \end{cases} \quad (10)$$

Exponential and logarithmic maps. The exponential and logarithmic maps in the pseudo-hyperboloid manifold are defined as $\exp_{\mathbf{x}} : \mathcal{T}_{\mathbf{x}}\mathcal{Q}_{\beta}^{s,t} \rightarrow \mathcal{Q}_{\beta}^{s,t}$ and $\log_{\mathbf{x}} : \mathcal{Q}_{\beta}^{s,t} \rightarrow \mathcal{T}_{\mathbf{x}}\mathcal{Q}_{\beta}^{s,t}$, respectively. We have the following closed form expressions of the exponential and the logarithmic maps [19], which allow us to perform operations on points on the pseudo-hyperboloid or pseudo-sphere manifolds

by mapping them to *tangent* spaces and vice-versa, formally given by

$$\exp_{\mathbf{x}}(\xi) = \begin{cases} \cosh\left(\frac{\sqrt{\langle \xi, \xi \rangle}}{\sqrt{|\beta|}}\right) \mathbf{x} + \frac{\sqrt{|\beta|}}{\sqrt{\langle \xi, \xi \rangle}} \sinh\left(\frac{t\sqrt{\langle \xi, \xi \rangle}}{\sqrt{|\beta|}}\right) \xi, & \text{if } \langle \xi, \xi \rangle > 0 \\ \mathbf{x} + \xi, & \text{if } \langle \xi, \xi \rangle = 0 \\ \cos\left(\frac{\sqrt{\langle \xi, \xi \rangle}}{\sqrt{|\beta|}}\right) \mathbf{x} + \frac{\sqrt{|\beta|}}{\sqrt{\langle \xi, \xi \rangle}} \sin\left(\frac{t\sqrt{\langle \xi, \xi \rangle}}{\sqrt{|\beta|}}\right) \xi, & \text{if } \langle \xi, \xi \rangle < 0 \end{cases} \quad (11)$$

$$\log_{\mathbf{x}}(\mathbf{y}) = \begin{cases} \frac{\cosh^{-1}\left(\frac{\langle \mathbf{x}, \mathbf{y} \rangle_t}{\beta}\right)}{\sqrt{\left(\frac{\langle \mathbf{x}, \mathbf{y} \rangle_t}{\beta}\right)^2 - 1}} \left(\mathbf{y} - \frac{\langle \mathbf{x}, \mathbf{y} \rangle_t}{\beta} \mathbf{x}\right), & \text{if } \frac{\langle \mathbf{x}, \mathbf{y} \rangle_t}{|\beta|} < -1 \\ \mathbf{y} - \mathbf{x}, & \text{if } \frac{\langle \mathbf{x}, \mathbf{y} \rangle_t}{|\beta|} = -1 \\ \frac{\cos^{-1}\left(\frac{\langle \mathbf{x}, \mathbf{y} \rangle_t}{\beta}\right)}{\sqrt{1 - \left(\frac{\langle \mathbf{x}, \mathbf{y} \rangle_t}{\beta}\right)^2}} \left(\mathbf{y} - \frac{\langle \mathbf{x}, \mathbf{y} \rangle_t}{\beta} \mathbf{x}\right), & \text{if } \frac{\langle \mathbf{x}, \mathbf{y} \rangle_t}{|\beta|} \in (-1, 1) \end{cases} \quad (12)$$

It is worth mentioning that not all points on the pseudo-hyperboloid manifold are connected by a geodesic. For these broken points, there does not exist a tangent vector ξ such that $\mathbf{y} = \exp_{\mathbf{x}}(\xi)$. Namely, the logarithmic map is not defined if $\langle \mathbf{x}, \mathbf{y} \rangle \geq |\beta|$.

Distance. By the means of the geodesic, the distance between \mathbf{x} and \mathbf{y} in semi-Riemannian manifolds $\mathcal{Q}_{\beta}^{s,t}$ is defined as the arc length of geodesic $\gamma(\tau)$, given by Eq. (13).

$$d(\mathbf{x}, \mathbf{y}) = \sqrt{\left\| \log_{\mathbf{x}}(\mathbf{y}) \right\|_t^2}. \quad (13)$$

Parallel Transport. Given the geodesic $\gamma(\tau)$ on $\mathcal{Q}_{\beta}^{s,t}$ passing through $\mathbf{x} \in \mathcal{Q}_{\beta}^{s,t}$ with the tangent direction $\xi \in \mathcal{T}_{\mathbf{x}}\mathcal{Q}_{\beta}^{s,t}$, the parallel transport of $\zeta \in \mathcal{T}_{\mathbf{x}}\mathcal{Q}_{\beta}^{s,t}$ is defined as Eq. (14).

$$P_{\mathbf{x} \rightarrow \mathbf{y}}^{\beta}(\xi) = \begin{cases} \frac{\langle \zeta, \xi \rangle}{\|\xi\|} \left[\mathbf{x} \sinh(\tau \|\xi\|) + \frac{\xi}{\|\xi\|} \cosh(\tau \|\xi\|) \right] + \left(\zeta - \frac{\langle \zeta, \xi \rangle}{\|\xi\|^2} \xi \right), & \text{if } \langle \xi, \xi \rangle > 0 \\ \frac{\langle \zeta, \xi \rangle}{\|\xi\|} \left[\mathbf{x} \sin(\tau \|\xi\|) - \frac{\xi}{\|\xi\|} \cos(\tau \|\xi\|) \right] + \left(\zeta + \frac{\langle \zeta, \xi \rangle}{\|\xi\|^2} \xi \right), & \text{if } \langle \xi, \xi \rangle < 0 \\ \langle \zeta, \xi \rangle \left(\tau \mathbf{x} + \frac{1}{2} \tau^2 \xi \right) + \zeta, & \text{otherwise} \end{cases} \quad (14)$$

where $\xi = \log_{\mathbf{x}}(\mathbf{y})$.

D Review of Riemannian Geometry

We briefly review some basic notions of Riemannian geometry, product manifolds and relevant geodesic tools. Refer [41, 42, 43] for more details.

Manifold/Differential Geometry. A smooth manifold (\mathcal{M}, g) is defined as a smooth manifold equipped with a metric g , which induces a scalar product for each point $\mathbf{x} \in \mathcal{M}$ on the *tangent* space $\mathcal{T}_{\mathbf{x}}\mathcal{M}$. For each point \mathbf{x} , the metric tensor is defined as $g_{\mathbf{x}} : \mathcal{T}_{\mathbf{x}}\mathcal{M} \times \mathcal{T}_{\mathbf{x}}\mathcal{M} \rightarrow \mathbb{R}$, which varies smoothly with the point \mathbf{x} and induces geometric notions such as geodesic distances, angles and curvatures.

Riemannian Manifold. A Riemannian Manifold (\mathcal{M}, g) is a manifold \mathcal{M} equipped with a Riemannian metric g . The Riemannian metric is positive definite that means $\forall \xi \in \mathcal{T}_{\mathbf{x}}\mathcal{M}, g_{\mathbf{x}}(\xi, \xi) > 0$ iff $\xi \neq 0$. We denote the *curvature* of a manifold as K and different notions of *curvature* quantify the ways in which a surface is locally curved around a point. There are three different types of constant curvature Riemannian manifold \mathcal{M} with respect to the sign of curvature: hyperboloid \mathbb{H}_K (negative curvature), hypersphere \mathbb{S}_K (positive curvature) and Euclidean space \mathbb{R} (zero curvature).

$$\mathcal{M} = \begin{cases} \mathbb{S}_K^n = \{\mathbf{x} \in \mathbb{R}^{n+1} : \langle \mathbf{x}, \mathbf{x} \rangle_2 = 1/K\}, & \text{if } K > 0 \\ \mathbb{E}^n = \mathbb{R}^n, & \text{if } K = 0 \\ \mathbb{H}_K^n = \{\mathbf{x} \in \mathbb{R}^{n+1} : \langle \mathbf{x}, \mathbf{x} \rangle_{\mathcal{L}} = 1/K\}, & \text{if } K < 0 \end{cases} \quad (15)$$

where $\langle \cdot, \cdot \rangle_2$ is the standard Euclidean inner product, and $\langle \cdot, \cdot \rangle_{\mathcal{L}}$ is the Lorentz inner product. For $\forall \mathbf{x}, \mathbf{y} \in \mathbb{R}^{n+1}$, the Lorentz inner product $\langle \mathbf{x}, \mathbf{y} \rangle_{\mathcal{L}}$ is defined as follows.

$$\langle \mathbf{x}, \mathbf{y} \rangle_{\mathcal{L}} = -x_1 y_1 + \sum_{i=2}^{n+1} x_i y_i, \quad (16)$$

Product Manifolds. Given a sequence of smooth manifolds M_1, M_2, \dots, M_k , the product manifold [16] is defined as the Cartesian product $M = M_1 \times M_2 \times \dots \times M_k$, with the metric tensor $g(\mathbf{u}, \mathbf{v}) = \sum_{i=1}^k g_i(u_i, v_i)$. Correspondingly, the points $\mathbf{x} \in \mathcal{M}$ can be represented as their coordinates $\mathbf{x} = (x_1, \dots, x_k)$, $x_i \in \mathcal{M}_i$.

Geodesics. A smooth curve γ of minimal length between two points \mathbf{x} and \mathbf{y} is called a geodesic [12, 43], which can be seen as the generalization of a straight-line in Euclidean space. Formally, the geodesic is defined as $\gamma_{\mathbf{x} \rightarrow \boldsymbol{\xi}}(\tau) : I \rightarrow \mathcal{M}$ from an interval $I = [0, 1]$ of the reals to the metric space \mathcal{M} , which maps a real value $\tau \in I$ to a point on the manifold \mathcal{M} with initial velocity $\boldsymbol{\xi} \in \mathcal{T}_{\mathbf{x}}\mathcal{M}$. By the means of geodesic, the exponential map can be defined as $\exp_{\mathbf{x}}(\boldsymbol{\xi}) = \gamma_{\mathbf{x} \rightarrow \boldsymbol{\xi}}(1)$.

Exponential and logarithmic map in Riemannian manifold. The connections between manifolds and *tangent* space are established by the differentiable exponential map and logarithmic map. The exponential map $\exp_{\mathbf{x}}$ at \mathbf{x} gives a way to project back a vector $\mathbf{v} \in \mathcal{T}_{\mathbf{x}}\mathcal{M}$ to a point $\exp_{\mathbf{x}}(\mathbf{v}) \in \mathcal{M}$ on the manifold. And the logarithmic map $\log_{\mathbf{x}} : \mathcal{M} \rightarrow \mathcal{T}_{\mathbf{x}}\mathcal{M}$ is defined as the inverse of the exponential map. Common realizations of Riemannian manifolds are hypersphere \mathbb{S}_K , the Euclidean space \mathbb{R} , and the hyperboloid \mathbb{H}_K . And we summarize *expmap* and *logmap* operations in these three spaces compactly in Table 5. For more detailed operations in Riemannian manifold, refer to [42].

Table 5: Summary of *expmap* and *logmap* in \mathbb{R} , \mathbb{S}_K and \mathbb{H}_K .

Operations	
<i>expmap</i> in \mathbb{R}	$\exp_{\mathbf{x}}(\mathbf{v}) = \mathbf{x} + \mathbf{v}$
<i>logmap</i> in \mathbb{R}	$\log_{\mathbf{x}}(\mathbf{y}) = \mathbf{y} - \mathbf{x}$
<i>expmap</i> in \mathbb{S}_K	$\exp_{\mathbf{x}}^K(\mathbf{v}) = \cos\left(\sqrt{ K }\ \mathbf{v}\ _2\right) + \sin\left(\sqrt{ K }\ \mathbf{v}\ _2\right) \frac{\mathbf{v}}{\sqrt{ K }\ \mathbf{v}\ _2}$
<i>logmap</i> in \mathbb{S}_K	$\log_{\mathbf{x}}^K(\mathbf{y}) = \frac{\cos^{-1}(K\langle \mathbf{x}, \mathbf{y} \rangle_2)}{\sqrt{1-K^2\langle \mathbf{x}, \mathbf{y} \rangle_2^2}} (\mathbf{y} - K\langle \mathbf{x}, \mathbf{y} \rangle_2 \mathbf{x})$
<i>expmap</i> in \mathbb{H}_K	$\exp_{\mathbf{x}}^K(\mathbf{v}) = \cosh\left(\sqrt{ K }\ \mathbf{v}\ _{\mathcal{L}}\right) \mathbf{x} + \sinh\left(\sqrt{ K }\ \mathbf{v}\ _{\mathcal{L}}\right) \frac{\mathbf{v}}{\sqrt{ K }\ \mathbf{v}\ _{\mathcal{L}}}$
<i>logmap</i> in \mathbb{H}_K	$\log_{\mathbf{x}}^K(\mathbf{y}) = \frac{\cosh^{-1}(K\langle \mathbf{x}, \mathbf{y} \rangle_{\mathcal{L}})}{\sqrt{K^2\langle \mathbf{x}, \mathbf{y} \rangle_{\mathcal{L}}^2 - 1}} (\mathbf{y} - K\langle \mathbf{x}, \mathbf{y} \rangle_{\mathcal{L}} \mathbf{x})$

E Proof of Theorems

E.1 Proof of Theorem 3.1

Theorem 3.1 (Theorem 4.1 in [19]). *For any point $\mathbf{x} \in \mathcal{Q}_{\beta}^{s,t}$, there exists a diffeomorphism $\psi : \mathcal{Q}_{\beta}^{s,t} \rightarrow \mathbb{S}_1^t \times \mathbb{R}^s$ that maps \mathbf{x} into the product manifolds of an unit sphere and the Euclidean space, the mapping and its inverse are given by,*

$$\psi(\mathbf{x}) = \left(\frac{\frac{1}{\|\mathbf{t}\|}\mathbf{t}}{\frac{1}{\sqrt{|\beta|}}\mathbf{s}} \right) \quad \text{and} \quad \psi^{-1}(\mathbf{z}) = \sqrt{|\beta|} \begin{pmatrix} \sqrt{1 + \frac{\|\mathbf{v}\|^2}{\|\mathbf{u}\|^2}} \mathbf{u} \\ \mathbf{v} \end{pmatrix}, \quad (17)$$

where $\mathbf{x} = \begin{pmatrix} \mathbf{t} \\ \mathbf{s} \end{pmatrix} \in \mathcal{Q}_{\beta}^{s,t}$ with $\mathbf{t} \in \mathbb{R}_*^{t+1}$ and $\mathbf{s} \in \mathbb{R}^s$. $\mathbf{z} = \begin{pmatrix} \mathbf{u} \\ \mathbf{v} \end{pmatrix} \in \mathbb{S}_1^t \times \mathbb{R}^s$ with $\mathbf{u} \in \mathbb{S}_1^t$ and $\mathbf{v} \in \mathbb{R}^s$.

Please refer Appendix C.5 in [19] for proof of this theorem.

E.2 Proof of Theorem 3.2

Theorem 3.2. *For any point $\mathbf{x} \in \mathcal{Q}_{\beta}^{s,t}$, there exists a diffeomorphism $\psi : \mathcal{Q}_{\beta}^{s,t} \rightarrow \mathbb{S}_{-\beta}^t \times \mathbb{R}^s$ that maps \mathbf{x} into the product manifolds of a sphere and the Euclidean space, the mapping and its inverse are given by,*

$$\psi(\mathbf{x}) = \begin{pmatrix} \sqrt{|\beta|} \frac{\mathbf{t}}{\|\mathbf{t}\|} \\ \mathbf{s} \end{pmatrix} \quad \text{and} \quad \psi^{-1}(\mathbf{z}) = \begin{pmatrix} \frac{\sqrt{|\beta| + \|\mathbf{v}\|^2}}{\sqrt{|\beta|}} \mathbf{u} \\ \mathbf{v} \end{pmatrix}, \quad (18)$$

where $\mathbf{x} = \begin{pmatrix} \mathbf{t} \\ \mathbf{s} \end{pmatrix} \in \mathcal{Q}_\beta^{s,t}$ with $\mathbf{t} \in \mathbb{R}_*^t$ and $\mathbf{s} \in \mathbb{R}^s$. $\mathbf{z} = \begin{pmatrix} \mathbf{u} \\ \mathbf{v} \end{pmatrix} \in \mathbb{S}_{-\beta}^t \times \mathbb{R}^s$ with $\mathbf{u} \in \mathbb{S}_{-\beta}^t$ and $\mathbf{v} \in \mathbb{R}^s$.

Proof. We need to show that $\psi(\psi^{-1}(\mathbf{z})) = \mathbf{z}$ and $\psi^{-1}(\psi(\mathbf{x})) = \mathbf{x}$. Here, we consider space dimensions and time dimensions separately.

For space dimensions, the mapping of the space dimensions of \mathbf{x} to the space dimensions of \mathbf{z} is an identity function (i.e. $\mathbf{v} = \mathbf{s}, \mathbf{s} = \mathbf{v}$). Thus, we only need to show the invertibility of the mappings taking time dimensions as inputs.

For time dimensions, we first show that:

$$\psi^{-1}(\psi(\mathbf{t})) = \frac{\sqrt{|\beta| + \|\mathbf{v}\|^2}}{\sqrt{|\beta|}} \sqrt{|\beta|} \frac{\mathbf{t}}{\|\mathbf{t}\|} = \sqrt{|\beta| + \|\mathbf{v}\|^2} \frac{\mathbf{t}}{\|\mathbf{t}\|} = \sqrt{|\beta| + \|\mathbf{s}\|^2} \frac{\mathbf{t}}{\|\mathbf{t}\|} = \|\mathbf{t}\| \frac{\mathbf{t}}{\|\mathbf{t}\|} = \mathbf{t}. \quad (19)$$

Note that the last equality can be inferred by the fact that $\mathbf{x} \in \mathcal{Q}_\beta^{s,t}$ and $\beta < 0$. We then show that:

$$\psi(\psi^{-1}(\mathbf{u})) = \sqrt{|\beta|} \frac{\sqrt{|\beta| + \|\mathbf{v}\|^2}}{\sqrt{|\beta|}} \frac{\mathbf{u}}{\|\frac{\sqrt{|\beta| + \|\mathbf{v}\|^2}}{\sqrt{|\beta|}} \mathbf{u}\|} = \sqrt{|\beta|} \frac{\mathbf{u}}{\|\mathbf{u}\|} = \mathbf{u}. \quad (20)$$

Note that the last equality can be inferred by the fact that $\mathbf{u} \in \mathbb{S}_{-\beta}^t$ and $\beta < 0$. \square

E.3 Proof of Theorem 3.3

Theorem 3.3. For any point $\mathbf{x} \in \mathcal{Q}_\beta^{s,t}$, there exists a diffeomorphism $\psi : \mathcal{Q}_\beta^{s,t} \rightarrow \mathbb{R}^{t-1} \times \mathbb{H}_\beta^{s+1}$ that maps \mathbf{x} into the product manifolds of the Euclidean space and hyperboloid, the mapping and its inverse are given by,

$$\psi(\mathbf{x}) = \begin{pmatrix} \mathbf{t} \\ \text{sign}(\mathbf{h}) \sqrt{|\beta| + \|\mathbf{s}\|^2} \\ \mathbf{s} \end{pmatrix} \quad \text{and} \quad \psi^{-1}(\mathbf{z}) = \begin{pmatrix} \mathbf{u} \\ \text{sign}(\mathbf{w}) \sqrt{\|\mathbf{w}\|^2 - \|\mathbf{u}\|^2} \\ \mathbf{v} \end{pmatrix}, \quad (21)$$

where $\mathbf{x} = \begin{pmatrix} \mathbf{t} \\ \mathbf{h} \\ \mathbf{s} \end{pmatrix} \in \mathcal{Q}_\beta^{s,t}$ with $\mathbf{t} \in \mathbb{R}_*^{t-1}$, $\mathbf{h} \in \mathbb{R}_*^1$ and $\mathbf{s} \in \mathbb{R}^s$. $\mathbf{z} = \begin{pmatrix} \mathbf{u} \\ \mathbf{w} \\ \mathbf{v} \end{pmatrix} \in \mathbb{R}^{t-1} \times \mathbb{H}_\beta^{s+1}$ with $\mathbf{u} \in \mathbb{R}^{t-1}$ and $\begin{pmatrix} \mathbf{w} \\ \mathbf{v} \end{pmatrix} \in \mathbb{H}_\beta^{s+1}$.

Proof. Let us first check that ψ and ψ^{-1} are well-defined and smooth. The main problem is to see that $\sqrt{\|\mathbf{w}\|^2 - \|\mathbf{u}\|^2}$ and its mixed partial derivatives of all orders exist and are continuous

at every point. This is the case if $\|\mathbf{w}\|^2 - \|\mathbf{u}\|^2 > 0$. Note that if $\mathbf{z} = \begin{pmatrix} \mathbf{u} \\ \mathbf{w} \\ \mathbf{v} \end{pmatrix}$ is in the range

of ψ , that is, $\mathbf{z} \in \psi(\mathcal{Q}_\beta^{s,t})$, then there is an $\mathbf{x} = \begin{pmatrix} \mathbf{t} \\ \mathbf{h} \\ \mathbf{s} \end{pmatrix} \in \mathcal{Q}_\beta^{s,t}$ such that $\mathbf{u} = \mathbf{t}, \mathbf{v} = \mathbf{s}, \mathbf{w} =$

$\text{sign}(\mathbf{h}) \sqrt{|\beta| + \|\mathbf{s}\|^2}$. By definition of $\mathcal{Q}_\beta^{s,t}$, we have $-\|\mathbf{t}\|^2 - \|\mathbf{h}\|^2 + \|\mathbf{s}\|^2 = \beta < 0$. Therefore, $\|\mathbf{w}\|^2 - \|\mathbf{u}\|^2 = \|\text{sign}(\mathbf{h}) \sqrt{|\beta| + \|\mathbf{s}\|^2}\|^2 - \|\mathbf{t}\|^2 = |\beta| + \|\mathbf{s}\|^2 + \beta - \|\mathbf{s}\|^2 + \|\mathbf{h}\|^2 = \|\mathbf{h}\|^2 > 0$ since $\mathbf{h} \in \mathbb{R}_*^1$.

It remains to show that $\psi(\psi^{-1}(\mathbf{z})) = \mathbf{z}$ and $\psi^{-1}(\psi(\mathbf{x})) = \mathbf{x}$. Without loss of generality, we consider the upper-sheet hyperboloid ($\mathbf{h} > 0, \mathbf{w} > 0$). We have

$$\psi^{-1}(\psi(\mathbf{x})) = \psi^{-1} \left(\begin{pmatrix} \mathbf{t} \\ \sqrt{|\beta| + \|\mathbf{s}\|^2} \\ \mathbf{s} \end{pmatrix} \right) = \begin{pmatrix} \mathbf{t} \\ \sqrt{\|\mathbf{t}\|^2 + \|\mathbf{s}\|^2 - \|\mathbf{t}\|^2} \\ \mathbf{s} \end{pmatrix} = \begin{pmatrix} \mathbf{t} \\ \mathbf{h} \\ \mathbf{s} \end{pmatrix} = \mathbf{x}. \quad (22)$$

For the second to last equality, note that the definition of $\mathcal{Q}_\beta^{s,t}$ implies that $\beta = \|\mathbf{x}\|_t^2 = -\|\mathbf{t}\|^2 - \|\mathbf{h}\|^2 + \|\mathbf{s}\|^2$. Since $\beta < 0$ and $\mathbf{h} > 0$, we have $\mathbf{h} = \sqrt{|\beta| + \beta + \|\mathbf{h}\|^2} = \sqrt{|\beta| + \|\mathbf{s}\|^2 - \|\mathbf{t}\|^2}$. Furthermore,

$$\psi(\psi^{-1}(\mathbf{z})) = \psi^{-1} \left(\left(\begin{array}{c} \mathbf{u} \\ \sqrt{\|\mathbf{w}\|^2 - \|\mathbf{u}\|^2} \\ \mathbf{v} \end{array} \right) \right) = \psi^{-1} \left(\left(\begin{array}{c} \mathbf{u} \\ \sqrt{|\beta| + \|\mathbf{v}\|^2} \\ \mathbf{v} \end{array} \right) \right) = \left(\begin{array}{c} \mathbf{u} \\ \mathbf{w} \\ \mathbf{v} \end{array} \right) = \mathbf{z}. \quad (23)$$

For the second to last equality, note that $\left(\begin{array}{c} \mathbf{w} \\ \mathbf{v} \end{array} \right) \in \mathbb{H}_\beta^{s+1}$. Thus, we have $\beta = -\|\mathbf{w}\|^2 + \|\mathbf{v}\|^2$ and since $\beta < 0$, $\|\mathbf{w}\|^2 = |\beta| + \|\mathbf{v}\|^2$.

The corresponding statement can be proven for the lower-sheet hyperboloid ($\mathbf{h} < 0, \mathbf{w} < 0$) by changing the signs. \square

E.4 Proof of Theorem 3.4

Theorem 3.4. *For any point $\mathbf{x} \in \mathcal{Q}_\beta^{s,t}$ ($s > 0, t > 1$), and two integers $a \in [0, s], b \in [1, t]$, there exists a diffeomorphism $\psi : \mathcal{Q}_\beta^{s,t} \rightarrow \mathbb{R}^{t-b} \times \mathcal{Q}_\beta^{a,b} \times \mathbb{R}^{s-a}$ that maps $\mathcal{Q}_\beta^{s,t}$ to the product manifolds of the Euclidean space and its submanifold.*

Proof. First note that \simeq is an equivalence relation. Reflexivity and symmetry follow immediately from the definition, for transitivity note that diffeomorphisms are closed under function composition, that is, if $f : U \rightarrow V$ and $g : V \rightarrow W$ are diffeomorphisms, then so is $h : U \rightarrow W$ defined by $h = g \circ f$. Hence, $U \simeq V$ and $V \simeq W$ imply $U \simeq W$. Note also that if $U \simeq V$, then $\mathbb{R}^{d_1} \times U \times \mathbb{R}^{d_2} \simeq \mathbb{R}^{d_1} \times V \times \mathbb{R}^{d_2}$ for all $d_1, d_2 \in \mathbb{N}_0$. Using Theorem 3.2 and 3.3, we get

$$\begin{aligned} \mathbb{R}^{t-b} \times \mathcal{Q}_\beta^{a,b} \times \mathbb{R}^{s-a} &\simeq \mathbb{R}^{t-b} \times \mathbb{S}_\beta^b \times \mathbb{R}^a \times \mathbb{R}^{s-a} && (\text{Theorem 3.2}) \\ &= \mathbb{R}^{t-b} \times \mathbb{S}_\beta^b \times \mathbb{R}^s \\ &\simeq \mathbb{R}^{t-b} \times \mathcal{Q}_\beta^{s,b} && (\text{Theorem 3.2}) \\ &\simeq \mathbb{R}^{t-b} \times \mathbb{R}^{b-1} \times \mathbb{H}_\beta^{s+1} && (\text{Theorem 3.3}) \\ &= \mathbb{R}^{t-1} \times \mathbb{H}_\beta^{s+1} \\ &\simeq \mathcal{Q}_\beta^{s,t}. && (\text{Theorem 3.3}) \end{aligned}$$

\square

E.5 Proof of Theorem 3.5

Theorem 3.5. *For the pseudo-hyperboloid $\mathcal{Q}_\beta^{s,t}$ ($s > 0, t > 1$), the corresponding diffeomorphic manifold $\mathbb{R}^{t-b} \times \mathcal{Q}_\beta^{a,b} \times \mathbb{R}^{s-a}$ is g -connected iff $a = 0$ and $b \in (1, t]$.*

Proof. Since \mathbb{R} is a g -connected space. The g -connectedness of $\mathbb{R}^{t-b} \times \mathcal{Q}_\beta^{a,b} \times \mathbb{R}^{s-a}$ can be proved by checking the g -connectedness of the component $\mathcal{Q}_\beta^{a,b}$. We consider different cases of $\mathcal{Q}_\beta^{a,b}$ with varying settings of $a \in [0, s]$ and $b \in [1, t]$.

For $a \in (0, s]$ and $b \in (1, t]$, the component $\mathcal{Q}_\beta^{a,b}$ is a pseudo-hyperboloid, which is connected but not g -connected.

For $a \in (0, s]$ and $b = 1$, the component $\mathcal{Q}_\beta^{a,b}$ is a (double-sheet) hyperboloid containing two isolated connected sheets, and these two sheets are not even connected.

For $a = 0$ and $b = 1$, the component $\mathcal{Q}_\beta^{a,b}$ is a 0-sphere consisting of two isolated points, which is

²Note that $\mathbb{R}^{t-b} \times \mathcal{Q}_\beta^{a,b} \times \mathbb{R}^{s-a} = \mathcal{Q}_\beta^{a,b} \times \mathbb{R}^{s+t-a-b}$ by exchanging the dimensions, we use the former one to preserve the order of the dimension in the diffeomorphism.

not connected.

For $a = 0$ and $b \in (1, t]$, the component $\mathcal{Q}_\beta^{a,b}$ is a q -sphere with $q = b - 1$, which is obviously g -connected. \square

E.6 Proof of Theorem 3.6

Theorem 3.6. *For any reference point $\mathbf{x} = \begin{pmatrix} \mathbf{t} \\ \mathbf{s} \end{pmatrix} \in \mathcal{Q}_\beta^{s,t}$ with space dimension $\mathbf{s} = \mathbf{0}$, the induced tangent space of $\mathcal{Q}_\beta^{s,t}$ is equal to the tangent space of its diffeomorphic manifold $\mathbb{S}_{-\beta}^t \times \mathbb{R}^s$, namely, $\mathcal{T}_{\psi(\mathbf{x})}(\mathbb{S}_{-\beta}^t \times \mathbb{R}^s) = \mathcal{T}_\mathbf{x} \mathcal{Q}_\beta^{s,t}$.*

Proof. For any point $\mathbf{x} = \begin{pmatrix} \mathbf{t} \\ \mathbf{s} \end{pmatrix} \in \mathcal{Q}_\beta^{s,t}$ with $\mathbf{s} = \mathbf{0}$, the corresponding point in the diffeomorphic manifold is $\psi(\mathbf{x}) = \begin{pmatrix} \sqrt{|\beta|} \frac{\mathbf{t}}{\|\mathbf{t}\|} \\ \mathbf{0} \end{pmatrix}$. Based on the definition of tangent space, for any tangent vector $\xi \in \mathcal{T}_\mathbf{x} \mathcal{Q}_\beta^{s,t}$, $\langle \mathbf{x}, \xi \rangle_t = 0$ implies $-\mathbf{t}\xi_t + \mathbf{0}\xi_s = 0$, which means $\mathbf{t}\xi_t = 0$. Thus, $\langle \psi(\mathbf{x}), \xi \rangle_t = 0$. Based on the definition of tangent space, $\xi \in \mathcal{T}_{\psi(\mathbf{x})}(\mathbb{S}_{-\beta}^t \times \mathbb{R}^s)$. \square

E.7 Proof of Theorem 3.7

Theorem 3.7. *For any point $\mathbf{x} \in \mathcal{Q}_\beta^{s,t}$, the union of the normal neighborhood of \mathbf{x} and the normal neighborhood of its antipodal point $-\mathbf{x}$ cover the entire manifold. Namely, $\mathcal{U}_\mathbf{x} \cup \mathcal{U}_{-\mathbf{x}} = \mathcal{Q}_\beta^{s,t}$.*

Proof. For any point $\mathbf{x} \in \mathcal{Q}_\beta^{s,t}$ and $\mathbf{y} \notin \mathcal{U}_\mathbf{x}$. Based on the definition of normal neighborhood, $\langle \mathbf{x}, \mathbf{y} \rangle_t \geq |\beta| \rightarrow \langle -\mathbf{x}, \mathbf{y} \rangle_t \leq |\beta|$. Thus, $\mathbf{y} \in \mathcal{U}_{-\mathbf{x}}$, and $\mathcal{U}_\mathbf{x} \cup \mathcal{U}_{-\mathbf{x}} = \mathcal{Q}_\beta^{s,t}$. \square

F Additional Theorem

F.1 Diffeomorphism of 0-Sphere

We give the special case of Theorem 3.4 by setting $a = 0, b = 1$.

Theorem F.1. *For any point $\mathbf{x} \in \mathcal{Q}_\beta^{s,t}$, there exists a diffeomorphism $\psi : \mathcal{Q}_\beta^{s,t} \rightarrow \mathbb{R}^{t-1} \times \mathbb{S}^0 \times \mathbb{R}^s$ that maps \mathbf{x} into the product manifold of Euclidean and 0-sphere.³*

F.2 Trainable curvature

Similar to the trainable curvature in the hyperbolic space [27], we give an analogue of Theorem 4.1 in [27] as following corollary.

Corollary F.1. *For any two points $\mathbf{x}, \mathbf{y} \in \mathcal{Q}_\beta^{s,t}$, there exists a mapping $\phi : \mathcal{Q}_\beta^{s,t} \rightarrow \mathcal{Q}_{\beta'}^{s,t}$ that maps \mathbf{x}, \mathbf{y} into $\mathbf{x}', \mathbf{y}' \in \mathcal{Q}_{\beta'}^{s,t}$, such that the semi-Riemannian inner product is scaled by a constant factor $\frac{\beta'}{\beta}$. Namely $\langle \mathbf{x}, \mathbf{y} \rangle_t = \frac{\beta'}{\beta} \langle \mathbf{x}', \mathbf{y}' \rangle_t$. The mapping is given by $\phi(\mathbf{x}) = \sqrt{\frac{\beta'}{\beta}} \mathbf{x}$.*

Corollary F.1 shows that assuming infinite machine precision, pseudo-hyperboloids of varying curvatures should have the same expressive power. However, due to the limited machine precision [27], we set the curvature $1/\beta$ as a trainable parameter to capture the best scale of the embeddings.

³The 0-sphere is the 0-manifold consisting of two points, which is not even connected.

G Experimental Details and Analyses

In this section, we present the details of our experiments and implementations, as well as some additional analyses.

G.1 Dataset Analysis

Table 6 and Table 7 summarize the statistics of the datasets we used for our experiments. Besides, we measure the graph sectional curvature to identify the dominating geometry of each dataset. Fig. 5 shows the histograms of sectional curvature and the mean sectional curvature for all datasets. It can be seen that all datasets have both positive and negative sectional curvatures, showcasing that all graphs contain mixed geometric structures. However, the datasets possess a preference for the negative half sectional curvature except the case of Facebook that has dominating positive sectional curvature, showcasing that most of real-world graphs exhibit more hierarchical structures than cyclic structures. To further analyze the degree of hierarchy of each graph, we apply δ -hyperbolicity to identify the tree-likeness. Table 8 shows the δ -hyperbolicity of different datasets. It shows that although most of the datasets have negative mean sectional curvature, their degrees of hierarchy vary significantly. For example, Airport and Pubmed are more hierarchical than CiteSeer and Cora.

Table 6: A summary of characteristics of the datasets for graph reconstruction. For each dataset, we report the number of nodes and the number of edges.

Dataset	Power	Bio-Worm	Web-Edu	Facebook
#Nodes	4941	2274	3031	4039
#Edges	6594	78328	6474	88234

Table 7: A summary of characteristics of the datasets for node classification and link prediction. For each dataset, we report the number of nodes, the number of edges, the number of classes and the feature dimensions.

Dataset	Airport	Pubmed	CiteSeer	Cora
#Nodes	3188	19717	3327	2708
#Edges	18631	44338	4732	5429
#Classes	4	3	6	7
#Features	4	500	3703	1433

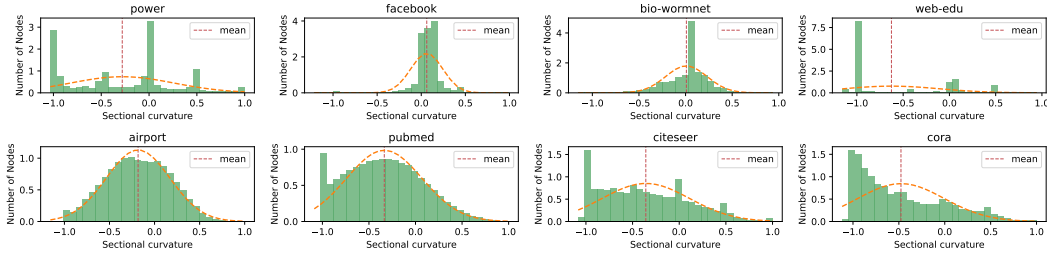


Figure 5: The histograms of sectional curvature for all used datasets.

G.2 Graph Reconstruction

For graph reconstruction, one straightforward method is to minimize the graph distortion [28, 16] given by

$$\frac{1}{|V|^2} \sum_{u,v} \left(\left(\frac{d(u,v)}{d_G(u,v)} \right)^2 - 1 \right)^2, \quad (24)$$

Table 8: The δ -hyperbolicity distribution of all used datasets.

Datasets	0	0.5	1.0	1.5	2.0	2.5	3.0
Power	0.4025	0.1722	0.1436	0.0773	0.0639	0.0439	0.0388
Bio-Worm	0.5635	0.3949	0.0410	0	0	0	0
Web-Edu	0.9532	0.0468	0	0	0	0	0
Facebook	0.8209	0.1569	0.0221	0	0	0	0
Airport	0.6376	0.3563	0.0061000	0	0	0	0
Pubmed	0.4239	0.4549	0.1094	0.0112	0.00060	0	0
CiteSeer	0.3659	0.3538	0.1699	0.0678	0.0288	0	0
Cora	0.4474	0.4073	0.1248	0.0189	0.0016	0.0102	0

where $d(\mathbf{u}, \mathbf{v})$ is the distance function in the embedding space and $d_G(u, v)$ is the graph distance (the length of shortest path) between node u and v , $|V|$ is the number of nodes in graph. The objective function is to preserve all pairwise graph distances. Motivated by the fact that most of graphs are partially observable, we minimize an alternative loss function [19, 35] that preserves local graph distance, given by,

$$\mathcal{L}(\Theta) = \sum_{(u,v) \in \mathcal{D}} \log \frac{e^{-d(\mathbf{u}, \mathbf{v})}}{\sum_{\mathbf{v}' \in \mathcal{E}(u)} \exp^{-d(\mathbf{u}, \mathbf{v}')}}, \quad (25)$$

where \mathcal{D} is the connected relations in the graph, $\mathcal{E}(u) = \{v | (u, v) \notin D \cup u\}$ is the set of negative examples for node u , $d(\mathbf{u}, \mathbf{v})$ is the distance function in the embedding space. For evaluation, we apply the mean average precision (mAP) to evaluate the graph reconstruction task. mAP is a local metric that measures the average proportion of the nearest points of a node which are actually its neighbors in the original graph. The mAP is defined as Eq. (26).

$$\text{mAP}(f) = \frac{1}{|V|} \sum_{u \in V} \frac{1}{\deg(u)} \sum_{i=1}^{|\mathcal{N}_u|} \frac{|\mathcal{N}_u \cap R_{u,v_i}|}{|R_{u,v_i}|}, \quad (26)$$

where f is the embedding function, $|V|$ is the number of nodes in graph, $\deg(u)$ is the degree of node u , \mathcal{N}_u is the one-hop neighborhoods in the graph, $R_{u,v}$ denotes whether two nodes u and v are connected.

G.3 Link Prediction

For link prediction, we use the Fermi-Dirac decoder to model the probability of an edge as proposed by [8], formally given by Eq. (27)

$$P(e_{uv} \in \mathcal{E} | \Theta) = \frac{1}{e^{(d(\mathbf{u}, \mathbf{v}) - r)/t} + 1}, \quad (27)$$

where r and t are hyperparameters, $d(\mathbf{u}, \mathbf{v})$ is the distance function in the embedding space.

G.4 Implementation Details

We implement our models by Pytorch and *GeoOpt* tool⁴. Our models and baselines are built upon the codes⁵. For baselines of product space and κ -GCN, we use the code⁶. Our models are trained on NVIDIA A100 with 4 GPU cards. Similar to [27], we use the pre-trained embeddings on link prediction as the initialization of node classification, to preserve graph structures information. All non-Euclidean methods do not use attention mechanism for a fair comparison.

Optimization. Although our model and embeddings are learned in pseudo-hyperboloid, the trainable parameters (linear transformation weight, bias, curvatures) are defined in Euclidean space, thus can be optimized via Euclidean optimization by applying diffeomorphic *expmap* and *logmap*. Similar to [27], we use Adam optimizer with early stopping to optimize the parameters.

⁴<https://github.com/geoopt/geoopt>

⁵<https://github.com/HazyResearch/hgcn>, <https://github.com/CheriseZhu/GIL>

⁶<https://github.com/fal025/producthgcn>

Numerical instability. In practice, we find that the numerical computation in pseudo-hyperboloid is not stable due to the limited machine precision and rounding. To ensure the learned embeddings to remain on the manifold, we perform a differentiable mapping $\varphi : \mathbb{R}_*^{t+1} \times \mathbb{R}^s \rightarrow \mathcal{Q}_\beta^{s,t}$ that can be composed of the diffeomorphisms from Theorem 3.2 or 3.3. The intuition is that we treat the embeddings that are not located on the manifold as Euclidean feature and map them into the diffeomorphic manifolds $\mathbb{S}_{-\beta}^t \times \mathbb{R}^s$ (or $\mathbb{R}^{t-1} \times \mathbb{H}_\beta^{s+1}$) via $\psi(\cdot)$ and then map it into the pseudo-hyperboloid $\mathcal{Q}_\beta^{s,t}$ via $\psi^{-1}(\cdot)$, where ψ can be instantiated by Lemma 3.2 or Lemma 3.3.

To ensure the tangent vectors to remain on the tangent space, we conduct projection operations via Eq. (28) after each vector operations.

$$\Pi_{\mathbf{x}}(\mathbf{z}) = \mathbf{z} - \frac{\langle \mathbf{z}, \mathbf{x} \rangle_t}{\langle \mathbf{x}, \mathbf{x} \rangle_t} \mathbf{x}, \quad (28)$$

where \mathbf{z} is the tangent vector to be projected.

Skip connection. In preliminary experiments of graph reconstruction, we found that the performance of GCN, HGCN, κ -GCN and \mathcal{Q} -GCN could not compete with the method in [16] that directly optimizes the distance function. We hypothesized that this was probably caused by over-smoothing of graph convolution kernel. Therefore, we decided to apply skip-connection strategy [44, 45, 46] to avoid oversmoothing. Specifically, we take the mean of the hidden output of each layer to the decoder. Table 1 reports the graph reconstruction results of GCN, HGCN, κ -GCN and \mathcal{Q} -GCN applied with skip-connection.

Hyperparameters settings. For node classification and link prediction, the optimal hyper-parameters are obtained by grid search. The ranges of grid search are summarized in Table 9.

Table 9: The grid search space for the hyperparameters.

Hyperparameter	Search space
Number of layers	1,2,3
Weight decay	0, 1e-3, 5e-4, 1e-4
Dropout rate	0,0.1,0.2,0.3,0.4,0.5,0.6,0.7
Activation	relu, tanh, sigmoid, elu

G.5 Computation Efficiency

The time complexity is the same as a vanilla GCN given by $O(|V|dd' + |E|d')$, where $|V|$ and $|E|$ are the number of nodes and edges, d and d' are the dimension of input and hidden features. The computation can be parallelized across all nodes. Similar to other non-Euclidean GCNs [27, 28, 14], the mapping operations from manifolds to the tangent space consume additional computation resources, compared with Euclidean GCNs.

Table 10 shows that \mathcal{Q} -GCN achieves higher efficiency than Prod-GCN ($\mathbb{H}^5 \times \mathbb{S}^5$). This is mainly owing to that the component \mathbb{R} in our diffeomorphic manifold ($\mathbb{S} \times \mathbb{R}$) runs faster than non-Euclidean components in $\mathbb{H}^5 \times \mathbb{S}^5$. Since the additional running time mainly comes from the mapping operations and we project the time dimensions to \mathbb{S} , the running time grows with the increase of the number of time dimensions. Overall, albeit slower than Euclidean GCN, the running time of all variants of \mathcal{Q} -GCN is smaller than the twice of time in Euclidean GCN, which is within the acceptable limits.

Table 10: The total running time (seconds) of graph reconstruction on Web-Edu and Facebook.

Manifolds	Web-Edu	Facebook
GCN (\mathbb{E}^{10})	2284	5456
Prod-GCN ($\mathbb{H}^5 \times \mathbb{S}^5$)	4336	10338
\mathcal{Q} -GCN ($\mathcal{Q}^{9,1}$)	2769	6981
\mathcal{Q} -GCN ($\mathcal{Q}^{7,3}$)	3363	6303
\mathcal{Q} -GCN ($\mathcal{Q}^{5,5}$)	3620	7142
\mathcal{Q} -GCN ($\mathcal{Q}^{3,7}$)	3685	7512
\mathcal{Q} -GCN ($\mathcal{Q}^{1,9}$)	3532	7980
\mathcal{Q} -GCN ($\mathcal{Q}^{0,10}$)	2778	7037